J Seismol
https://doi.org/10.1007/s10950-024-10241-4

RESEARCH

Fault imaging using earthquake sequences: a revised seismotectonic model for the Albstadt Shear Zone, Southwest Germany

Sarah Mader · Joachim R. R. Ritter · Andrea Brüstle · AlpArray Working Group

Received: 7 August 2023 / Accepted: 23 August 2024

Abstract In Germany, the highest seismic hazard is associated with the Albstadt Shear Zone (ASZ) in the western Swabian Jura, a low mountain range in southwest Germany. The region is affected by continuous micro-seismic activity with the potential for damaging earthquakes (nine events with $ML \geq 5$ in the 20^{th} century). Within the AlpArray and StressTransfer projects nine temporary seismic stations have been installed in the region of the ASZ to densify the permanent seismic monitoring. In October 2018 and September 2019, the state seismological survey (LED) detected two low-magnitude earthquake sequences with hundreds of events in the area. The temporarily densified local network allows us to systematically analyze these sequences and to search for other sequences by applying a template-matching routine on data from 2018 to 2020. In total, six earthquake sequences could be identified with at least 10 events. The four largest sequences ($>$ 50 events) consist of two fore- and aftershock sequence and two earthquake swarms. Earthquake swarms were so far not observed around the ASZ. Precise relative hypocenter relocations and the determination of fault-plane solutions allow us to propose a seismotectonic model based on the three imaged fault types: (a) The well-known NNE-SSW striking sinistral strike-slip ASZ at depths of 5-10 km, (b) a NW-SE striking dextral strike-slip fault zone at depths of 11-15 km beneath the Hohenzollerngraben (HZG), a shallow, apparently aseismic NW-SE striking graben structure; this NW-SE fault zone possibly is an inherited zone of weakness in the basement and facilitated the development of the HZG and (c) at the intersection of the ASZ with the NW-SE fault zone, complex faulting in form of NNW-SSE striking sinistral strike-slip and normal faulting possibly to accommodate local stresses.

Keywords Template-matching · Earthquake swarm · Relative hypocenter relocation · Fault-plane solutions

Article highlights

- First study of earthquake swarms in the area of the Albstadt Shear Zone, the most hazardous earthquake zone in Germany.
- Imaging of active faults with relative hypocenter relocations and fault-plane solutions.
- Observation of a new NW-SE striking fault zone below 11 km depth.

S. Mader (✉) · J. R. R. Ritter
KIT - Karlsruher Institute of Technology, Geophysical Institute, Hertzstr. 16, 76187 Karlsruhe, Baden-Württemberg, Germany
e-mail: sarah.mader@kit.edu

J. R. R. Ritter
e-mail: joachim.ritter@kit.edu

A. Brüstle
Regierungspräsidium Freiburg, Geological Survey of Baden-Württemberg, State Seismological Service, Alberstr. 5, 79104 Freiburg i. Br., Baden-Württemberg, Germany
e-mail: andrea.bruestle@led-bw.de

Published online: 13 September 2024

1 Introduction

In Central Europe intra-plate seismicity is driven by low deformation rates due to far-field tectonic processes (Müller et al. 1992, Piña-Valdés et al. 2022). This tectonic stress regime is especially related to the Alpine orogeny as well as to the Adriatic indenter and causes seismic activity preferably on faults, which are oriented favourably in the stress field (Reicherter et al. 2008, Röckel et al. 2022). The stress field in the northern Alpine foreland is mainly defined by extension parallel and compression perpendicular to the Alpine collision front, which is locally driven by the forces related with slab rollback of the European lithospheric slab (Kastrup et al. 2004, Kissling and Schlunegger 2018, Reinecker et al. 2010, Singer et al. 2014). The major seismically active faults in the northern Alpine foreland are the Albstadt Shear Zone (ASZ), the Freiburg-Bonndorf-Bodensee Fault Zone (FBBFZ) and the Upper Rhine Graben (Fig. 1), all favourably oriented in current stress field (Röckel et al. 2022). The reoccurrence times of strong, damaging earthquakes are in general up to several hundreds or even thousands of years (Hürtgen et al. 2020). Therefore, the study of regions with high micro-seismic activity is necessary to better understand the mechanisms and stresses related to intra-plate seismicity in the northern Alpine foreland. The ASZ in SW Germany (Fig. 1) provides a suitable study site, due to its frequent micro-seismic activity with mid-sized magnitude earthquakes and recurrence times of 20 - 30 years. Damaging earthquakes in this region are a major hazard (Grünthal et al. 2018), and risk studies estimate losses of several 100 million EURO related to residential buildings alone (Tyagunov et al. 2006). Such risks are quite reasonable if one recalls that the November 1911 Albstadt earthquake with a local magnitude (*ML*) of 6.1 and an intensity of EMS-98 VIII was felt about 400 km towards north in Germany and well into France, Switzerland, Austria and northern Italy (Schwarz et al. 2019, Sieberg and Lais 1925).

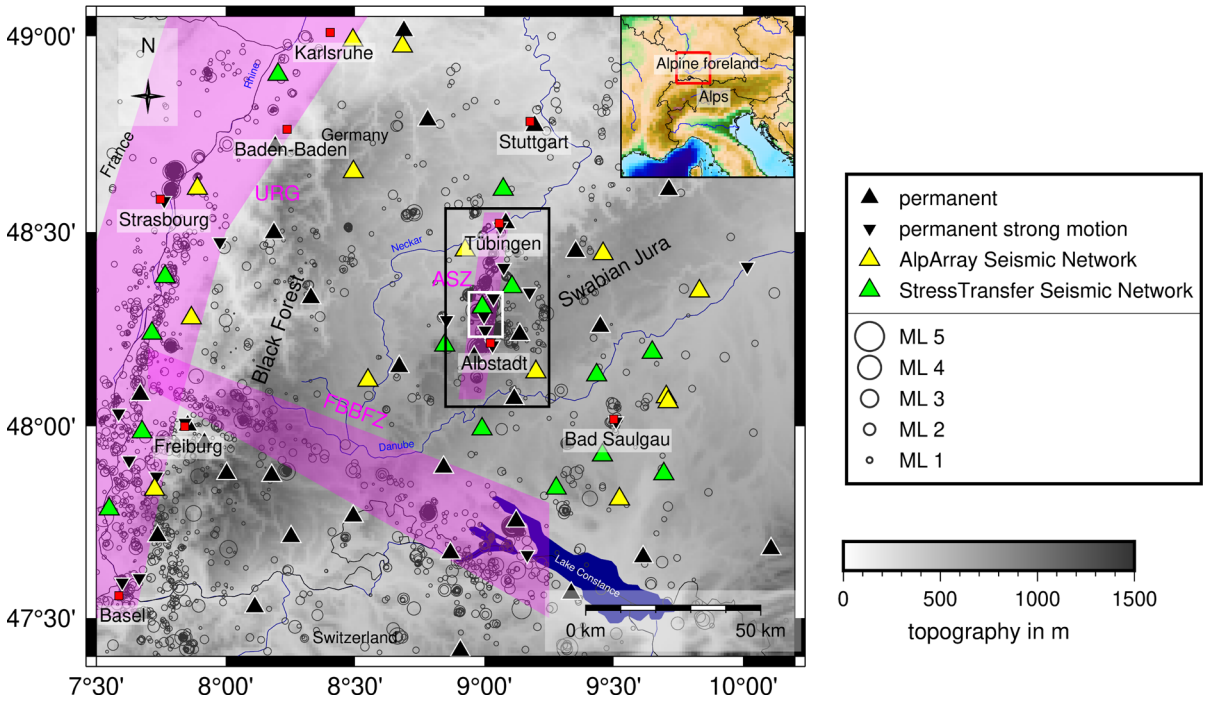

Fig. 1 Overview of the research area with seismic station distribution (triangles) during the studied time period and the epicenters of the LED event catalog from 2011 to 2020 (gray circles, Bulletin-Files des Landeserdbebendienstes B-W 2011-2020). The black frame surrounds the research area with the Albstadt Shear Zone (ASZ, magenta shaded area). The white frame borders the close-up area of Fig. 6. Other major fault systems are highlighted in magenta (URG = Upper Rhine Graben, FBBFZ = Freiburg-Bonndorf-Bodensee Fault Zone). Topography is based on SRTM15+ (Tozer et al. 2019). The inset gives the position within Central Europe

The ASZ is located in the Swabian Jura, a plateau-like mountain range composed of Jurassic limestone (Fig. 1). Continuous microseismic activity is documented since the 16th century with two major earthquakes near Tübingen in 1655 with intensities of EMS-98 VI or VII (Bulletin-Files des Landeserdbebendienstes B-W 2011-2020). Especially, since the occurrence of a *ML* 6.1 earthquake in 1911, several strong earthquakes with $ML \geq 5$ shook the region causing major damage in 1913 (*ML* ~5.6), 1924 (*ML* ~5.1), 1943 (*ML* ~5.5 and *ML* ~5.6), 1947 (*ML* ~5.0), 1969 (*ML* ~5.1), 1970 (*ML* ~5.2) and 1978 (*ML* ~5.7, Schwarz et al. 2019). Nevertheless, no morphological expression of the ASZ is visible at the Earth's surface. Seismotectonic analyses of the earthquakes revealed a NNE-SSW striking fault zone in the upper crust (Fig. 2, Mader et al. 2021, Reinecker and Schneider 2002, Stange and Brüstle 2005), but the NS extension of the ASZ is

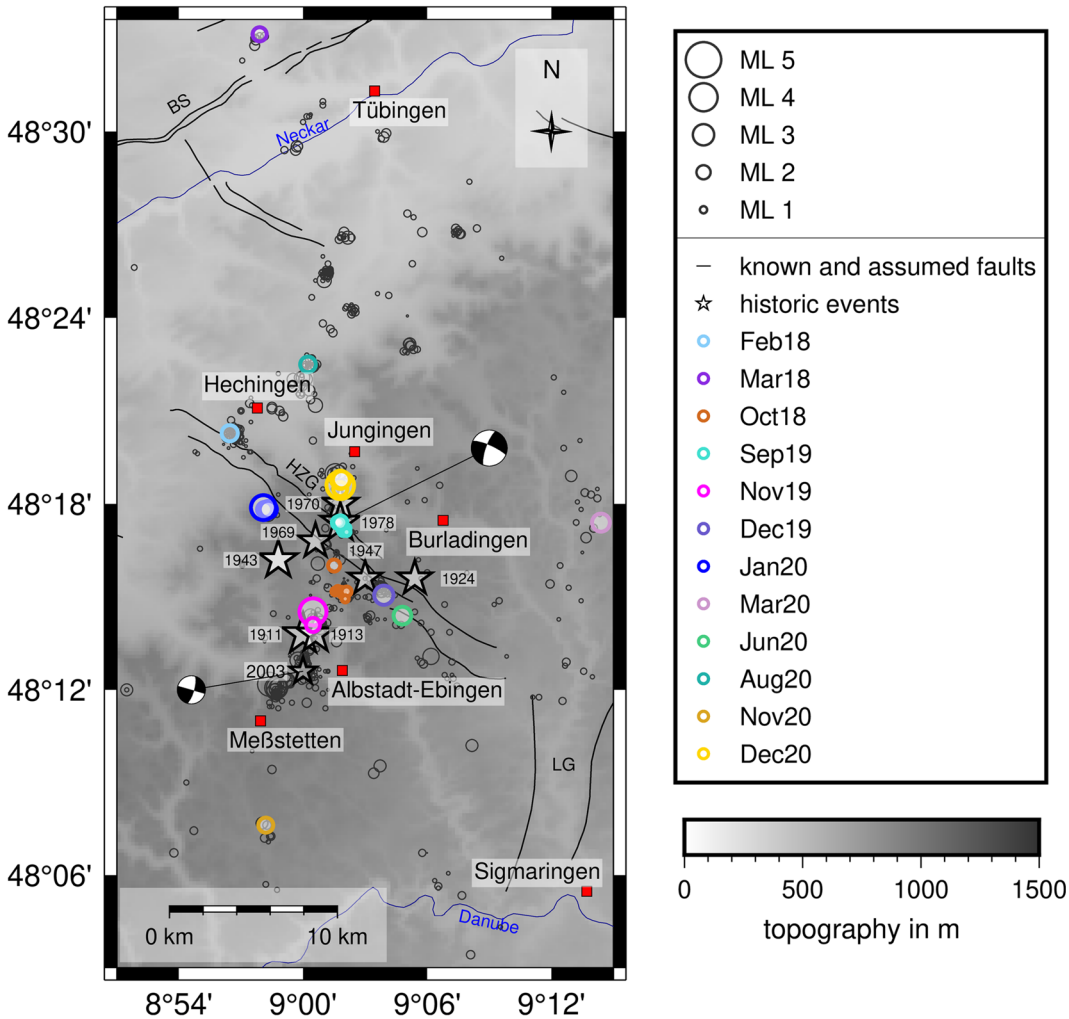

Fig. 2 Research area in the Swabian Jura. Gray circles indicate earthquake epicenters between 2011 and 2020 (LED event catalog, Bulletin-Files des Landeserdbebendienstes B-W 2011-2020). Stars represent important historic earthquakes with *ML* greater than 5 and the *ML* 4.4 earthquake in 2003 (Schwarz et al. 2019, Stange and Brüstle 2005). Fault planes solutions of the 1978 earthquake after Turnovsky (1981) and the 2003 earthquake after Stange and Brüstle (2005). Colored circles indicate epicenters of earthquakes used for the template-matching event detection. Black lines indicate faults in the area (BS = Bebenhausen Fault, HZG = Hohenzollerngraben, LG = Lauchertgraben, Regierungspräsidium Freiburg: Landesamt für Geologie, Rohstoffe und Bergbau (Hrsg.) 2019). Topography is based on SRTM15+ (Tozer et al. 2019)

still debated (e.g. Haessler et al. 1980, Reinecker and Schneider 2002, Stange and Brüstle 2005). The largest proposed extension of more than 120 km reaches from the Lake Constance to the North of the city of Stuttgart (Fig. 1, Reinecker and Schneider 2002). Stange and Brüstle (2005) and Mader et al. (2021) question this extension because the current seismic activity appears mainly limited to the area of the Swabian Jura (Fig. 1). Mader et al. (2021) suggest an extension of about 40 km between the towns Tübingen to the North and Meßstetten to the South, which is well outlined by the current seismic activity (Fig. 2). Fault-plane solutions of the *ML* 5.7 earthquake in 1978 and the *ML* 4.4 earthquake in 2003, as well as recent events indicate a dominant sinistral strike-slip faulting regime in a stress field with a maximum horizontal stress direction of $140° - 149°$ (Fig. 2, e.g., Haessler et al. 1980, Mader et al. 2021, Reiter et al. 2016, Stange and Brüstle 2005, Turnovsky 1981).

At the surface, the only visible tectonic structure is the Hohenzollerngraben (HZG), an about 25 km long NW-SE striking graben structure with an inverted relief, with the former graben now forming a topographic height (Fig. 2, Schädel 1976). Its depth range of about 2 - 3 km is based on the opening width of 1.5 km and the dip angles at the graben boundary faults of around 60° (Schädel 1976). A potential depth continuation of the graben boundary faults into the crystalline basement is unclear and still under discussion (Illies 1982, Reinecker and Schneider 2002). As there are several graben structures like the HZG to the north and south (e. g., Fildergraben, Rottenburg Flexure, western Lake Constance faults and Hegau, Reinecker and Schneider 2002), Reinecker and Schneider (2002) proposed a tectonic model for the ASZ, with a decoupling horizon. As a result, the movement of the ASZ in the crystalline basement is transferred as en-echelon graben structures to the surface, due to the partly decoupled horizon in between. As decoupling horizon, Reinecker and Schneider (2002) proposed the evaporites of the middle Muschelkalk, whereas Stange and Brüstle (2005) suggest a decoupling horizon directly above the crystalline basement. After Rupf and Nitsch (2008), the decoupling horizon would be located between 250 - 400 m depth close to the HZG. The thickness of the sedimentary cap rocks is about 1 km (Rupf and Nitsch 2008).

In October 2018, the state seismological service of Baden-Württemberg (LED, Bulletin-Files des Landeserdbebendienstes B-W 2011-2020) detected an earthquake sequence with more than 200 events in the area of the ASZ. In September 2019, another sequence with at least 800 earthquakes was identified by the LED at the closest seismic station. Such large earthquake sequences were so far not recorded in the region. Due to the large amount of very low magnitude earthquakes ($ML < 0.5$), a location of the majority of the detected events was not possible with the permanent seismic network (Bulletin-Files des Landeserdbebendienstes B-W 2011-2020).

The densification by the temporary seismic stations of the AlpArray (2016 - 2022, Hetényi et al. 2018) and the StressTransfer seismological experiments (since September 2018, Mader and Ritter 2021) in the area offers a unique opportunity to systematically analyse these two earthquake sequences and the local microseismic activity to image active fault structures (Fig. 1).

In this study, we use a multi-station template-matching detection routine with an automatic phase picking routine to detect and locate additional earthquakes. In this way, we can analyze small magnitude events, which are so far not included in the event catalog of the LED. We study the two time windows with known, unusually high seismic activity (October - November 2018 and September 2019) and time windows around events with a $ML \geq 2$ in the years 2018 to 2020 to search for other possible earthquake sequences and aftershocks. With the detected earthquake sequences, we aim to image the active fault planes by relative hypocenter relocations and identify the source mechanisms using fault-plane solutions.

2 Data

We use the waveform data of all available permanent seismic stations in up to about 100 km distance to the ASZ (Fig. 1). Permanent recordings are provided by the LED (Erdbebendienst Südwest Baden-Württemberg and Rheinland-Pfalz 2009), the Swiss Seismological Service (SED, Swiss Seismological Service (SED) at Eidgenössische Technische Hochschule (ETH) Zurich 1983), German Regional Seismic Network (GRSN, Federal Institute for Geosciences and Natural Resources (BGR) 1976) and GEOFON seismic network (GEOFON Data Centre 1993). This network of about 30 permanent seismic stations was densified by up to 10 seismic stations in the vicinity of

the ASZ (Fig. 1). The temporary seismic stations are part of the AlpArray Seismic Network (2015 - 2022, Hetényi et al. 2018) and the StressTransfer Seismic Network (September 2018 - 2030, Mader and Ritter 2021). The temporary densification reduced the maximum distance between broadband seismic stations to about 15 km (Mader and Ritter 2021).

Furthermore, the LED provided its event catalog (Bulletin-Files des Landeserdbebendienstes B-W 2011-2020), including origin time, hypocenter coordinates (Fig. 1), local magnitude *ML*, P as well as S phase arrival times and P phase polarities. The earthquakes *ML* range between 0.0 and 3.9 (Bulletin-Files des Landeserdbebendienstes B-W 2011-2020). Based on this event catalog, master events are defined for the template-matching event detection. The LED *ML* magnitudes are used as reference magnitudes for the relative magnitude estimation and the P phase polarities for the calculation of fault-plane solutions.

3 Methods

To find unknown events in the area of the Swabian Jura, we apply a template-matching detection routine with an automatic phase arrival time determination routine (Fig. 3). For the newly detected events, we determine the source parameters and calculate a relative magnitude to complement the LED event catalog. Finally, we calculate relative hypocenter relocations for the larger earthquake sequences to image the seismically active fault planes.

We use the LED earthquake catalog as starting point of our processing (Fig. 3, step 1: LED earthquake

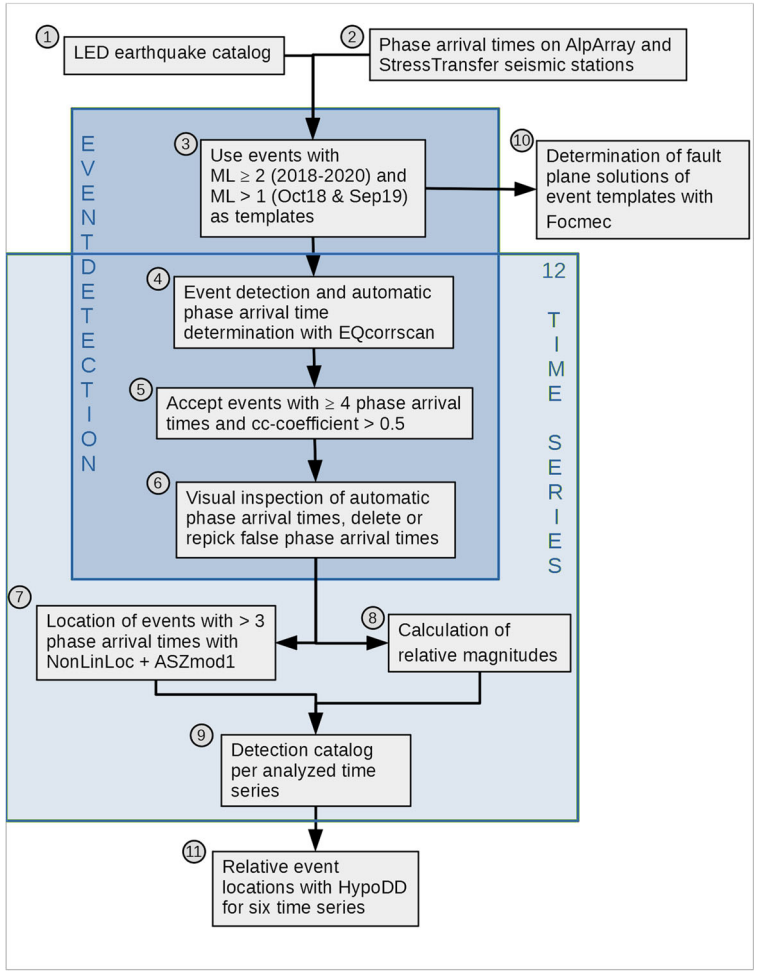

Fig. 3 Workflow for this work (1: LED earthquake catalog, 2: additional phase arrival times, 3: template selection, 4: template-matching detection, 5: detection filtering, 6: visual inspection, 7: event location, 8: relative magnitude estimation, 9: detection catalog, 10: fault-plane solutions, 11: relative hypocenter relocation) The 12 detection periods are listed in Table 1

catalog). We add direct P and S phase arrival times, as well as P and SH polarities, from the AlpArray and StressTransfer stations to the LED earthquake catalog to take advantage of the densified station network (Fig. 3, step 2: additional phase arrival times). In a next step, we select the events, which are used as waveform templates for the event detection process, from the complemented LED event catalog (Fig. 3, step 3: template selection). In total we select templates from 12 different time periods, which are further referred to as detection periods (Table 1). For each detection period we run a multi-station template-matching detector and automatically determine P and S phase arrival times using the Python package EQcorrscan (Chamberlain et al. 2018, Fig. 3, step 4: template-matching detection). The output is reduced to event detections with at least four reliable phase arrival times based on a cross-correlation coefficient (ccc) ≥ 0.5 (Fig. 3, step 5: detection filtering). To verify the correctness of the automatically determined phase arrival times, we visually inspect all phase arrival times and delete or repick false arrival times (Fig. 3, step 6: visual inspection). Finally, we complement the detection catalog of each detection period with the hypocenter and origin time by locating the events with NonLinLoc (Lomax et al. 2000), using the minimum 1-D seismic velocity model ASZmod1 (Mader et al. 2021, Fig. 3, step 7: event location), and the calculation of a relative event magnitude after Schaff and Richards (2014) (Fig. 3, step 8: relative magnitude estimation). Our processing steps lead to 12 detection catalogs from each analyzed detection period (Fig. 3, step 9: detection catalog, Table 1).

To identify the fault mechanism, we determine fault-plane solutions of the event templates using FOCMEC (Snoke 2003, Fig. 3, step 10: fault-plane solutions). Furthermore, we determine relative hypocenter relocations with HypoDD (Waldhauser and Ellsworth 2000) for the six detection catalogs, which feature at least ten events, to image the seismically active fault plane (Fig. 3, step 11: relative hypocenter relocation, Table 1).

3.1 Preprocessing

We preprocess all waveform data in the exactly same way to achieve a consistent dataset. The preprocessing is done for all processing steps which use the waveform data except the input creation of the additional phase arrival times and HypoDD cross-correlation differential-time data (Fig. 3, step 3: template selection, step 4: template-matching detection, step 5: detection filtering, step 6: visual inspection, step 8: relative magnitude estimation). We start with daylong time windows plus 30 s of continuous waveform data. The daylong time window is given by the software requierd by the EQcorrscan software, because the event detection routine is run day-wise. To ensure the detection of events around midnight, an overlap of 30 seconds is required. This overlap is based on twice the expected difference in arrival time at the closest and furthermost distant station. The waveform data is resampled to 50 Hz, to reduce the overall data size, detrended and filtered with a fourth-order Butterworth bandpass filter between 1 - 20 Hz. The waveform of an event or phase is extracted from the preprocessed waveform. For the input creation of the HypoDD cross-correlation differential-time data we used a sampling rate of 100 Hz, the data was also detrended and filtered with a fourth-order Butterworth bandpass filter between 1 - 20 Hz.

3.2 Additional phase arrival times

First, we determine the direct P and S phase onset times in the recordings of the six StressTransfer and four AlpArray seismic stations within our target region for events reported in the LED bulletin file (Fig. 1). This step was performed by applying the semi-automatic picking routine described in Mader et al. (2021) (Fig. 3, step 2: additional phase arrival times). An quality between 0 to 4 is assigned to an identified phase arrival time based on an automatically determined earliest and latest possible phase arrival time around the approximate phase onset time following procedures described by Diehl et al. (2012) and Mader et al. (2021), with details listed in Table 6. This results in 1073 additional phase arrival times complementing the LED event catalog in the years 2019 and 2020. For the year 2018, 569 phase arrival times at the AlpArray and StressTransfer seismic stations are taken from Mader et al. (2021), where the dataset was already processed in the same way.

3.3 Event detection

To identify additional microseismic earthquakes, we use the routines of the Python toolbox EQcorrscan

Table 1 Time overview, event templates and results for event detection for the 12 different detection periods

ID	time-period	templates time	magnitude *ML*	coordinates			number of detections	number of well located events	similar events in LED catalog	number of relative magnitudes	number of relative relocalized events
				° N	° E	depth in km					
Feb18	2018-01-31 - 2018-03-02	2018-02-10T12:44:38	2.3	48.33	8.95	13	23	17	4	15	12
Mar18	2018-02-28 - 2018-03-30	2018-03-10T21:16:33	2.0	48.55	8.98	15	1	1	1	1	–
Oct18	2018-10-01 - 2018-12-31	2018-10-15T10:14:42	1.1	48.25	9.04	10	220	150	71	154	113
		2018-10-15T15:01:43	1.2	48.25	9.05	9					
		2018-10-15T18:04:37	1.0	48.25	9.04	10					
		2018-10-15T19:37:35	1.3	48.25	9.04	10					
		2018-10-15T19:41:47	1.6	48.25	9.04	10					
		2018-10-17T03:02:32	1.0	48.25	9.04	10					
		2018-10-24T07:12:07	1.7	48.27	9.02	5					
		2018-11-25T02:22:18	1.4	48.25	9.06	13					
		2018-11-26T18:47:43	1.0	48.25	9.04	10					
Sep19	2019-09-01 - 2019-09-30	2019-09-08T16:12:48	1.1	48.27	9.06	11	590	319	59	280	228
		2019-09-08T16:22:44	1.7	48.29	9.04	12					

Table 1 continued

		2019-09-08T17:45:52	1.1	48.27	9.05	12					
		2019-09-09T01:49:08	1.5	48.28	9.05	12					
		2019-09-10T06:59:58	1.1	48.28	9.04	13					
		2019-09-10T07:00:31	1.1	48.29	9.04	13					
		2019-09-11T19:00:10	1.6	48.28	9.04	12					
		2019-09-19T03:19:20	2.0	48.28	9.05	12					
Nov19	2019-10-25 - 2019-11-24	2019-11-04T00:59:47	3.8	48.24	9.01	5	4	4	4	4	–
		2019-11-06T10:08:51	2.0	48.23	9.01	5					
Dec19	2019-11-25 - 2019-12-25	2019-12-05T10:14:17	2.7	48.25	9.07	5	3	3	1	3	–
Jan20	2020-01-17 - 2020-02-16	2020-01-27T03:48:22	2.1	48.29	8.98	11	411	297	108	251	243
		2020-01-27T22:05:25	2.4	48.29	8.98	11					
		2020-01-27T22:05:41	3.5	48.29	8.98	11					
Mar20	2020-02-25 - 2020-03-26	2020-03-06T19:10:41	2.5	48.29	9.24	7	3	2	1	3	–
Jun20	2020-06-08 - 2020-07-08	2020-06-18T22:41:12	2.5	48.23	9.09	7	2	2	1	2	–
Aug20	2020-08-02 - 2020-09-01	2020-08-12T18:42:19	2.2	48.37	9.01	10	4	3	1	4	–

Table 1 continued

Nov20	2020-11-07 - 2020-12-07	2020-11-17T07:20:23	2.1	48.12	8.98	6	17	13	8	12	13
Dec20	2020-11-20 - 2020-12-31	2020-11-30T23:25:46	3.9	48.31	9.04	8	74	63	23	42	47
		2020-12-01T01:59:13	2.0	48.31	9.04	8					
		2020-12-09T04:55:13	2.6	48.31	9.04	8					
		2020-12-25T15:10:33	2.4	48.31	9.04	8					

The resulting number of detected events with more than three phase arrival times have a ccc exceeding 0.5. The number of well-located events corresponds to events located with NonLinLoc (Lomax et al. 2000) with a horizontal and vertical location uncertainty of ≤ 2 km and at least 6 phase arrival times. The number of similar events in the LED catalog is based on the event sequence location and event time. All of those events within the LED catalog were detected with our approach

(Chamberlain et al. 2018) for our multi-station template-matching detection routine. As master events we choose all events with $ML \geq 2.0$ of the time period 2018-2020, to search for fore- and aftershock sequences. For the two time periods with known unusual earthquake sequences (October to November 2018 and September 2019) we choose a smaller *ML* threshold of $ML \geq 1.0$. The separation of the threshold is based on the information already known from the LED event catalog and the observations of the LED during our time period, as well as our focus on the earthquake sequences to image the active fault planes (Bulletin-Files des Landeserdbebendienstes B-W 2011-2020). Waveform templates are generated of each event that satisfies our selection criteria (see below, Table 1, Figs. 2 and 3, step 3: template selection). As we are interested in earthquake sequences, the event detection is executed around the origin time of the event template. Similar origin time (within $\pm$ 30 days) and location (within around 3 km) of event templates lead to a combination into one detection period. This leads to 12 separate detection periods (Table 1). The event detection process is run independently for each detection period and only the corresponding master event templates are used (Table 1).

As templates, we use the waveforms of direct P and S phases. P phases are detected on the vertical component Z and S phases on both horizontal components, N and E. The template has a length of 1.3 s and it begins 0.15 s before the actual phase arrival time. The waveform of the phase arrival time needs a minimum signal-to-noise ratio (SNR) of 7.5 to be accepted as a template waveform. The SNR is calculated as ratio between the maximum amplitude of the template waveform relative to the rms-amplitude of the whole time window. Finally, input templates are accepted only for earthquakes with at least three P phase waveforms on the vertical component and three S phase waveforms on the horizontal components satisfying the SNR criteria (Fig. 12).

For the template-matching event detection we apply the EQcorrscan function *match_filter* (Chamberlain et al. 2018, Fig. 3, step 4: template-matching detection). The continuous waveform data is prechecked for data gaps and corresponding days are skipped, if more than a third of the recording time is missing. The function *match_filter* determines a shifted stacked cross-correlation function (ccsum) for all waveforms. As detection threshold we use the Median Absolute Deviation ($MAD = threshold \cdot median(abs(cccsum))$) with a threshold value of 9, which is selected after some exemplary test runs to achieve a reasonable trade-off between true positive (seismic events) and false positive detections (unwanted signals). As we search with several master events with similar waveforms, we reject double detections within a second from different master events. In such case, we keep the detection with the highest ccsum value, after the detection process is completed for each 24 h plus 30 s time window. The detection process results in event catalogs per each analyzed day. Those event catalogs are combined to one detection catalog for each of the 12 time series after double detections due to the 30 s time overlap are rejected.

We use the EQcorrscan function *lag_calc* to determine automatic relative phase arrival times (Fig. 3, step 4: template-matching detection). P phase arrival times are determined on the Z-component and S phase arrival times on the horizontal components after Shelly and Hardebeck (2010) (Fig. 13). Only correlations between detection and template waveform with a ccc greater than 0.5 are accepted (Fig. 3, step 5: detection filtering). As our waveform templates begin 0.15 s before the actual phase arrival time, we correct the automatic relative phase arrivals for this time shift. Furthermore, we combine double S phase arrival times to one S phase arrival time, if they are found for the same station on both horizontal components. For this, we use the horizontal component with the higher ccc, if the determined arrival time differs for the N and E component. To assess an uncertainty to each phase arrival time, we convert the ccc to a time uncertainty following Table 2. The conversion was based on observations during the visual inspection (Fig. 3, step 6: visual inspection).

The following analysis is done for detected events with at least four automatic phase arrival times, as we want to locate the events at a later stage (Fig. 3, step 5: event filtering). To ensure the reliability of the automatic phase arrival times, we manually review all phase

Table 2 Cross-correlation coefficient (ccc) and corresponding time uncertainty of the detected phase arrival times

cross-correlation coefficient	time uncertainty in s
$ccc >= 0.8$	0.01
$0.6 <= ccc < 0.8$	0.05
$0.5 <= ccc < 0.6$	0.1

arrival times and sort out wrong ones, which corresponds to about 20% (Fig. 3, step 6: visual inspection). If problems like cycle shifts are detected, we revise the phases by hand. This is done for less than 1% (Fig. 3). For repicking, we again use the semi-automatic picking routine of Mader et al. (2021). After the visual inspection, events with three or less phase arrival times are kept in the detection catalog as valid events, which can not be localized (228 events).

The event detection results in 1070 additional earthquakes in comparison to the LED event catalog distributed in 12 detection catalogs, one for each analyzed detection period (Fig. 3, step 3 - 6, Table 1). The earthquakes used as templates, as well as earthquakes listed in the LED event catalog, are also included in those detection catalogs.

3.4 Event location

To complement the 12 detection catalogs with origin time and hypocenter coordinates, we relocate all events with at least 4 phase arrival times with the non-linear location algorithm NonLinLoc (Lomax et al. 2000) following Mader et al. (2021) (Fig. 3, step 7: event location, Fig. 4). As velocity model we use the local minimum 1-D seismic velocity model ASZ-mod1 and its corresponding station corrections, which was determined for the ASZ by Mader et al. (2021). In the same way, we relocate the LED event catalog of the years 2019 and 2020, supplemented with the phase arrival times from the AlpArray and StressTransfer seismic stations (Fig. 4). The relocated LED event catalog of the years 2011 to 2018 is taken from Mader et al. (2021).

3.5 Relative magnitude estimation

We use the method of Schaff and Richards (2014) to determine a relative magnitude for each event based on the comparison of the seismic phase amplitudes of template and detection waveforms (Fig. 3, step 8: relative magnitude estimation). Schaff and Richards (2014) introduce two possible ways to calculate relative magnitudes: (1) with correction terms for ccc and SNR (after equation 10, Schaff and Richards 2014) and (2) without correction terms, by applying the L2 norm of the amplitude ratio between slave and master event (equation 11, Schaff and Richards 2014). The master waveform corresponds to the waveform of the detection template and the slave waveform to the correspondingly detected waveform. Schaff and Richards (2014) suggest the first one to be a good choice for highly similar waveforms even with high noise conditions. Nevertheless, for low ccc like 0.5, a bias is introduced to the actual magnitude of up to 0.3 (Schaff and Richards 2014). This bias originates from dissimilar waveforms and noise on the master waveform. For this case, they introduce the calculation of relative magnitudes based on the ratio of the L2 norm. This calculation is insensitive onto bias due to the ccc but sensitive to high noise conditions. We decide to calculate our relative magnitudes based on the ratio of the L2 norm, because we kept phase arrival times with ccc values ≥ 0.5 in our event catalog and we also searched for aftershock events, which may have different source time functions or focal mechanisms. To account for the high sensitivity on noise during the relative magnitude calculation, we include only phase arrivals with a SNR > 3. As we have both, P and S phase arrival times, we modified the method of Schaff and Richards (2014) to determine a relative magnitude for both, P and S phases separately, using the waveform of the corresponding recording channel (Z for P and E or N for S). This leads to one relative magnitude for each phase and station combination for each event. The median of all station magnitude estimates per event is calculated to determine the overall relative magnitude of each event.

To analyze the stability of the relative event magnitude calculation and estimate its uncertainty range, we analyze the difference of the median magnitude minus the station magnitudes. For this, we determine the mean, median and the standard deviation of the difference between median and station magnitudes for different subsets. In these subsets, we vary the allowed minimum magnitude (0.1, 0.3, 0.5, 0.7, 1 or 1.5) and the allowed number of station magnitudes (at least 3, 5 or 10) used for the median magnitude calculation. For all subsets we observe a similar mean and median of zero and a standard deviation σ of 0.1 magnitude units (Fig. 14). This result demonstrates, that the method is very stable for all our magnitude determinations and that it is independent from the number of used station magnitudes, as well as site effects. Therefore, we determine also relative magnitudes based on only one station magnitude. We find $2\,\sigma$ to be a reasonable uncertainty estimate for our relative magnitudes as around 95% of our determinations lie within this range.

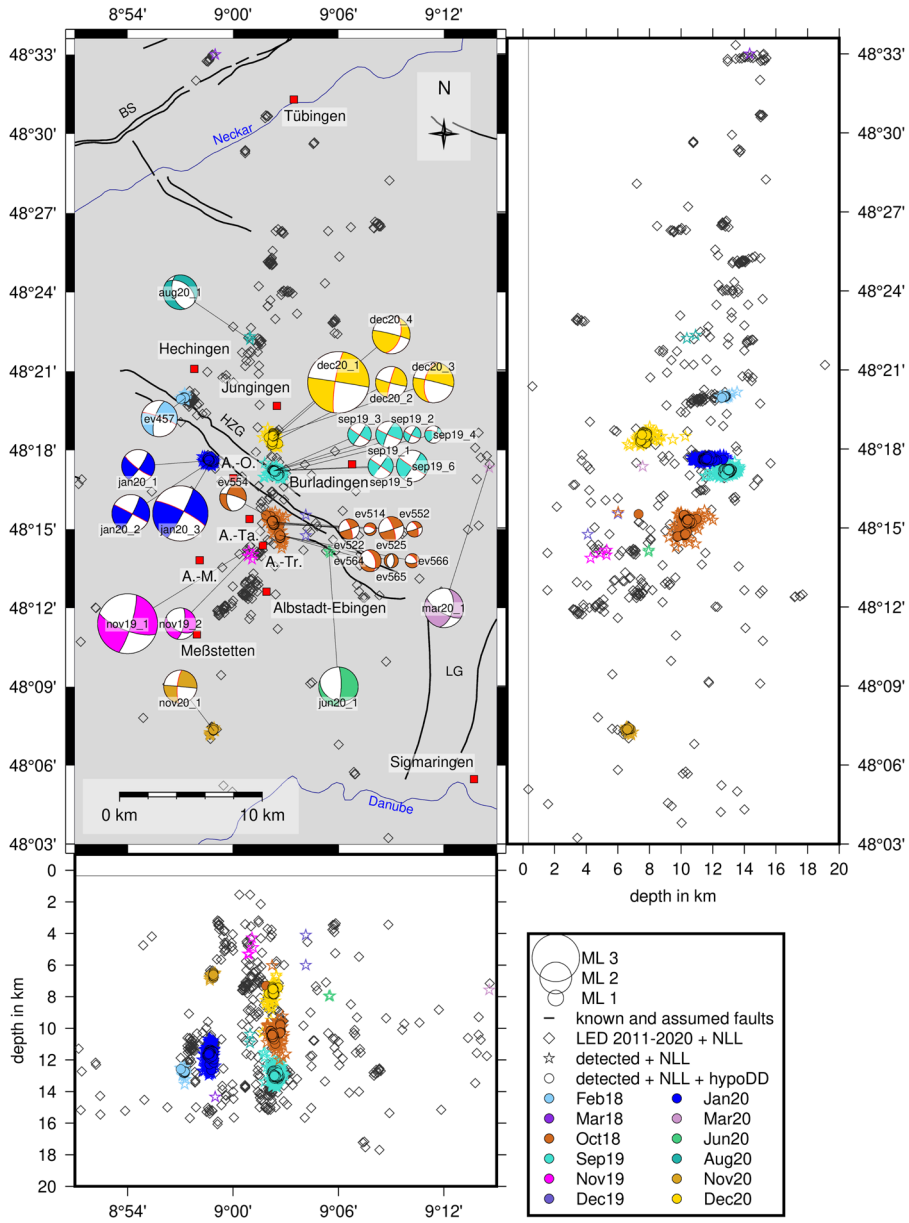

Fig. 4 HypoDD (circles) and NonLinLoc (stars, hypocenter uncertainty < 2 km and at least 6 phase picks) hypocenter locations of events detected by template-matching procedure, templates are included. Best localized earthquakes (diamonds) of the LED event catalog, localized in NonLinLoc using the velocity model ASZmod1 and station corrections (Mader et al. 2021). Localized events from 2011 to 2018 are taken from Mader et al. (2021) and complemented with newly located events in 2019 to 2020. Horizontal line in depth slices indicates in depth slices indicates approximate depth of the crystalline basement in the area of the ASZ (Rupf and Nitsch 2008). Ffault-plane solutions are scaled with magnitude as indicated in legend. (A.-O.: Albstadt-Onstmettingen, A.-Ta.: Albstadt-Tailfingen, A.-Tr.: Albstadt-Truchtelfingen, A.-M.: Albstadt-Margrethausen)

To compare our relative magnitudes with the LED *ML*, we determined the difference between both (Fig. 15). To interpret these differences, we have to consider all uncertainties of the magnitude values. The LED *ML* have a similar uncertainty range as our magnitudes of ±0.2 (Bulletin-Files des Landeserdbebendienstes B-W 2011-2020). If we consider the propagation of the uncertainties, we can expect a maximum difference between both magnitudes of ±0.6 within the measurement accuracy. We observe a good agreement with the LED magnitudes as most of the calculated differences are within ±0.6 magnitude values (Fig. 15). Only the Oct18 sequence contains a few events with absolute differences greater than 0.6. For those events, we control again the phase arrival times and waveforms, but we couldn't find an explanation for the larger differences visible in Fig. 15b.

In total, we determine a relative magnitude for 771 events (Table 1). We are not able to determine a relative magnitude for all events due to our SNR criterium, which is used to account for the noise sensitivity of the method.

3.6 Fault-plane solutions

The source mechanisms of our master events are calculated with FOCMEC (Snoke 2003) as described in Mader et al. (2021) based on P and SH polarities, as well as SH/P amplitude ratios (Table 3, Fig. 3, step 10: fault-plane solutions, Figs. 4, 6, and 16). The focal mechanisms of the 2018 time series are taken from Mader et al. (2021). We use the same quality assignment as in Mader et al. (2021) based on the width of the 5% to 95% percentile ranges of strike, dip and rake (δ strike, δ dip, δ rake, Table 3) for comparability (see Mader et al. 2021, Table A2). In total, we determined 19 fault-plane solutions ($1.1 \leq ML \leq 3.9$, Table 3).

3.7 Relative hypocenter relocation

Highly similar waveforms of the detected earthquakes within a time series indicate a possible common or similar fault plane and close-by hypocenter locations. To study this relationship, we use the double-difference earthquake relocation algorithm HypoDD (Waldhauser and Ellsworth 2000, Fig. 3, step 11: relative hypocenter relocation, Fig. 4). We determine relative hypocenter relocations for each of the 12 detection periods with at least 10 events (six earthquake sequences, Table 1). As input hypocenter locations for HypoDD we use the results of the event location with NLL. We use both, the relative phase arrival times of the detection catalog (ct) and the relative phase arrival times calculated with cross-correlation (cct) as combined input data set for HypoDD.

For the ct data, we convert our timing uncertainties into the weighting schema described in Table 4. To determine the ct times from our absolute phase arrival times, we use the HypoDD code ph2dt. The maximum hypocentral separation between two earthquakes was set to 10 km to ensure that all events within the catalog may be linked and all phase arrival times are accepted, independent of their pick weight. To become a neighboring event, only event pairs with at least eight links are accepted and a maximum of 50 links per event pair are allowed to keep the double-difference problem in a solvable size.

To create the cct input, we determine a list of all possible event pairs. If the distance between an event pair is larger than 5 km we reject the event pair. The neighboring events are checked for similar phase arrival times per station. The cross-correlation differential times (cct) are calculated in the time domain between the waveforms having phase arrival times and being sampled with 100 Hz. The median amplitude-squared coherence is used as a cct quality (Waldhauser and Ellsworth 2000). P phases are correlated on the Z-component and S phases are correlated on both horizontal components (N, E). The determined cct is used, if the median amplitude-squared coherence of the two correlated waveforms is greater than 0.5 in the frequency range between 1 - 20 Hz. If the cct of the S phase on the two horizontal components is identical, then the maximum of the estimated median amplitude-squared coherence is used as quality. Otherwise, the mean of the cct and the mean of the median amplitude-squared coherence of the two components are used as cct and cct quality.

To check if the result depends on the different input data types (P or S, ct or cct), we calculate the relative hypocenter relocations for different subsets, as shown in Fig. 5. Here, the result of the Sep19 sequence is displayed as an example, for the other five sequences see Figs. 17-21. We consider our solution as stable, if all subsets show similar hypocenter distibutions within around hundred meters. We always apply the conju-

Table 3 Input data to FOCMEC and parameters of the resulting solutions

ID	time	*ML*	° N	° E	depth in km	P	SH	SH/P	strike in °	dip in °	rake in °	δ strike in °	δ dip in °	δ rake in °	strike (aux) in °	dip (aux) in °	rake (aux) in °	quality
sep19_1	2019-09-08T16:23	1.7	48.29	9.04	11.99	25	8	2	114	86	169	13.1	23.7	28	205	79	4	2
sep19_2	2019-09-08T17:46	1.1	48.27	9.05	12.10	16	8	0	116	80	174	21.0	18.0	69.0	207	84	10	4
sep19_3	2019-09-09T01:49	1.5	48.28	9.05	12.37	25	9	3	123	86	-177	4.2	5.1	33.4	33	87	-4	2
sep19_4	2019-09-10T07:00	1.1	48.28	9.04	12.96	12	5	1	291	59	160	14.3	27.1	25.1	32	73	33	2
sep19_5	2019-09-11T19:00	1.6	48.28	9.04	12.44	29	8	2	305	90	-180	4.5	4.5	0.4	35	90	0	0
sep19_6	2019-09-19T03:20	2.0	48.28	9.05	12.29	32	9	4	123	86	-176	5.0	10.1	22.0	33	86	-4	2
nov19_1	2019-11-04T01:00	3.8	48.24	9.01	4.82	35	6	1	17	80	-19	5.2	11.5	20.0	110	71	-169	2
nov19_2	2019-11-06T10:09	2.0	48.23	9.01	4.83	28	3	1	12	71	-42	8.1	16.1	38.1	118	51	-155	3
jan20_1	2020-01-27T03:48	2.1	48.29	8.98	11.40	26	4	1	127	79	-169	0.0	0.0	0.0	35	79	-11	0
jan20_2	2020-01-27T22:05	2.4	48.29	8.98	11.18	28	4	2	298	89	173	7.1	15.5	24.3	28	83	1	2
jan20_3	2020-01-27T22:05	3.5	48.29	8.98	10.89	32	5	0	297	80	174	6.9	17.4	18.1	28	84	10	1
mar20_1	2020-03-06T19:10	2.5	48.29	9.24	7.37	34	5	1	13	52	-27	1.6	7.0	7.2	120	69	-139	0
jun20_1	2020-06-18T22:41	2.5	48.23	9.09	7.40	30	4	0	2	79	-62	0.3	3.5	5.0	112	30	-158	0
aug20_1	2020-08-12T18:42	2.2	48.37	9.01	10.04	33	5	1	164	53	-65	0.0	0.0	0.0	306	44	-119	0

Table 3 continued

nov20_1	2020-11-17T07:20	2.1	48.12	8.98	6.40	27	7	2	186	76	0	3.6	16.1	45.9	96	90	166	3
dec20_1	2020-11-30T23:26	3.9	48.31	9.04	7.65	37	5	1	189	81	-1	0.5	5.7	8.4	279	89	-171	0
dec20_2	2020-12-01T01:59	2.0	48.31	9.04	8.04	26	2	1	195	85	4	5.6	16.8	37.3	105	86	175	3
dec20_3	2020-12-09T04:55	2.6	48.31	9.04	7.80	31	4	1	191	55	-4	2.3	18.2	9.6	283	87	-145	1
dec20_4	2020-12-25T15:10	2.4	48.31	9.04	7.63	31	2	1	18	50	6	7.5	24.9	17	284	85	140	2
Mader et al. (2021)																		
ev457	2018-02-10T12:44	2.3	48.33	8.95	12.41	27	3	2	290	82	-160	2.0	6.9	19.0	197	70	-9	1
ev514	2018-10-15T18:46	0.8	48.25	9.04	10.35	8	4	1	289	61	-65	23.3	15.5	31.6	65	38	-127	3
ev522	2018-10-15T19:37	1.3	48.25	9.04	10.00	17	4	3	341	76	-1	2.8	6.8	10.2	71	89	-166	1
ev525	2018-10-15T19:41	1.6	48.25	9.04	10.08	27	4	4	341	75	-4	3.8	8.0	12.0	72	86	-165	1
ev552	2018-10-17T03:02	1.0	48.25	9.04	10.38	14	4	2	338	57	-7	9.3	32.0	11.4	72	84	-147	3
ev554	2018-10-24T07:12	1.7	48.27	9.03	5.22	23	4	2	185	50	-17	5.2	14.8	0.6	286	77	-139	1
ev564	2018-11-25T02:22	1.4	48.25	9.04	10.20	25	3	2	344	53	-65	0.0	0.0	0.0	126	44	-119	0
ev565	2018-11-25T07:36	0.9	48.25	9.04	10.24	21	2	0	190	35	-84	32.3	40.1	12.2	3	55	-94	4
ev566	2018-11-25T10:25	0.9	48.25	9.04	10.22	13	5	1	323	50	-45	35.3	15.6	14.5	86	57	-130	3

Values with (aux) refer to the assumed auxiliary fault plane. δ strike, δ dip and δ rake are the width of the 5% to 95% percentile range of strike, dip and rake and represent the uncertainty of the determined fault-plane solution

Table 4 Absolute uncertainty of the catalog phase arrival times and corresponding weighting value for HypoDD ct input

uncertainty time range in s	weighting value
$\|uncertainty\| <= 0.025$	1
$0.025 < \|uncertainty\| <= 0.05$	0.5
$0.05 < \|uncertainty\| <= 0.1$	0.2
$0.1 < \|uncertainty\| <= 0.2$	0.1
$0.2 < \|uncertainty\|$	0

gate gradient method (LSQR) to solve the double-difference equations. To get an estimate of the relative uncertainty, we run the singular value decomposition (SVD) on the combined P and S phase ct and P and S phase cct input data sets if possible. For larger data sets (event sequences Sep19 and Jan20), we run the SVD on a smaller subset, due to our maximum computing power. The maximum relative location uncertainty estimate is 90 m horizontally and 158 m vertically (see Table 5, also for median uncertainty estimates). The median SVD uncertainties tend usually to be unrealistically small (Truttmann et al. 2023). For this reason, we reported the maximum SVD uncertainties. Due to the small differences in hypocenter locations between the different subsets within all sequences, especially between the ct and cc data sets (Figs. 5, 17-21), we select as result the combined inversion of P and S phase ct and P and S phase cct starting from the NLL hypocenter locations. We run one set of inverstion with 10 iteration steps, without changing the weighting parameters of the ct and cct or other parameters during the inversion. A change of the weighting parameters between cc and ct data during the inver-

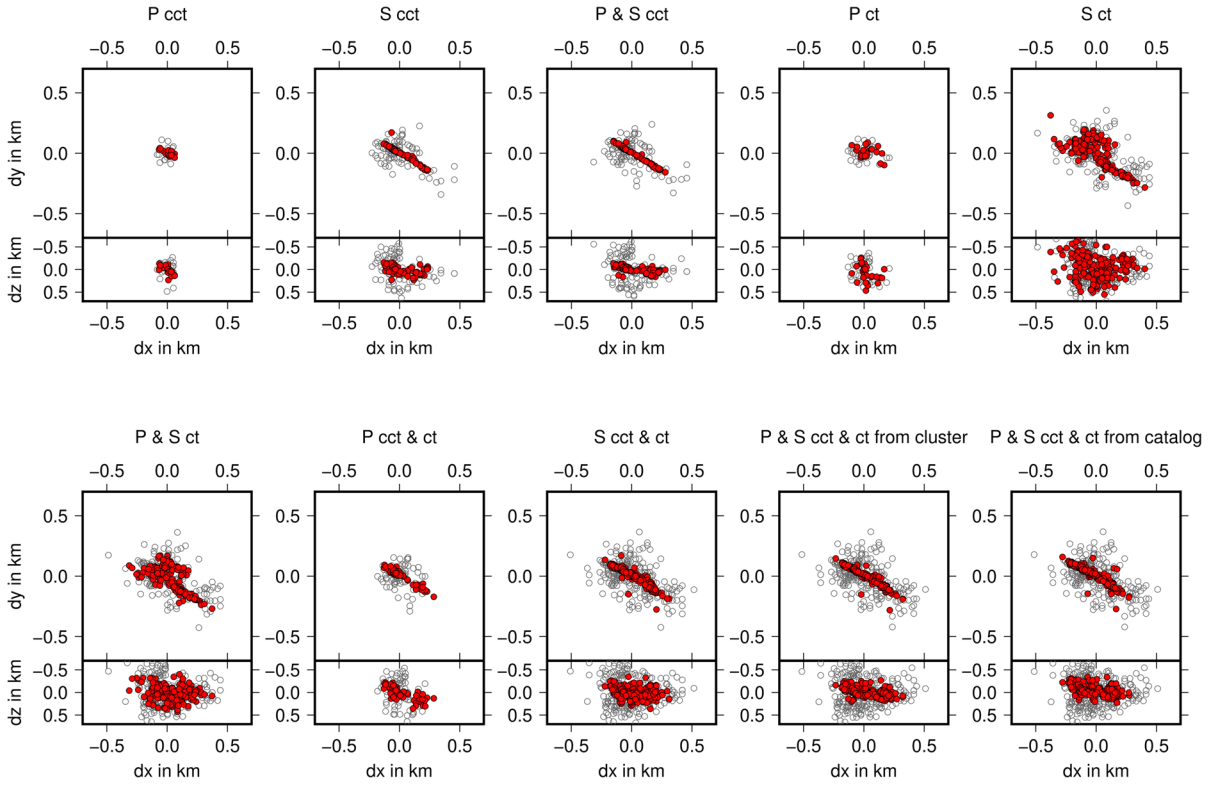

Fig. 5 Comparison of HypoDD performance with different data sets of the Sep19 earthquake sequence. Gray circles represent NLLoc hypocenter locations. Red filled circles show the result of HypoDD relative hypocenter relocations. Titles represent the data set used (ct=catalog times, cct=cross-correlation times, the starting point of the inversion can be either set to the hypocenter locations within the earthquake catalog or to the center of the cluster formed by the events.). Hypocenter locations are always displayed in map view and corresponding West-East depth slice below. The values along the x, y and z axes represent the distance to the cluster centroid position in km

Table 5 Uncertainty estimates of relative hypocenter relocations in x (ex), y (ey) and z (ez) distance based on HypoDD SVD run

ID	median ex in m	median ey in m	median ez in m	maximum ex in m	maximum ey in m	maximum ez in m
Feb18	14	10	25	65	50	95
Oct18	7	6	13	65	77	127
Sep19	7	9	16	43	40	53
Jan20	5	4	10	76	63	158
Nov20	5	4	12	20	12	28
Dec20	9	9	20	90	78	151

sion does not change the location and orientation of the imaged fault plane. An explanation may be, that the used catalog phase arrival times for the ct input data, are already determined by cross-correlation and not manually (Fig. 3).

4 Results

4.1 Detection catalog

We analyzed 12 detection periods from 2018 to 2020 including the majority of seismic activity in the area of the ASZ using a template-matching detection routine (Table 1). Six event catalogs of these detection periods are characterized by single events or less than ten events (Table 1). The remaining six detection periods contain the already known earthquake sequences from October to November 2018 and September 2019, as well as further earthquake sequences in February 2018 as well as in January, November, and December 2020 (Table 1). By applying this procedure, we have identified 1070 additional earthquakes in comparison to the LED event catalog. We were able to locate 840 earthquakes, from which 592 were classified as well located with a maximum location uncertainty of less than 2 km (horizontally and vertically) and at least six phase arrival times. In this way, we added more than twice the number of well located events to the LED event catalog for the analyzed time windows by applying the multi-station template-matching detection approach in combination with the densified station network (Table 1, Fig. 3). 656 earthquakes of the six observed earthquake sequences could be relocated relatively with HypoDD (Table 1). Furthermore, we determined relative magnitudes ranging from -0.6 up to 1.2 for 489 earthquakes of the newly detected events (Table 1). With the newly detected events, we complement the LED event catalog for our 12 detection periods, especially, for earthquakes of small magnitude (Fig. 22). The comparison of the magnitude-frequency distribution of the LED event catalog from 2018-2020 and the complemented LED catalog lead to a similar M_c of around 0.6 and a b-value close to 1 (0.9, Fig. 22). The similar M_c for both catalogs is due to our analysis approach. We only analyzed short time windows within the whole catalog period. An increased number of low magnitude events, however, occurs in the enhanced catalog (Fig. 22). This indicates that our strategy is successful and that it is possible to add well-located low-magnitude events to the LED event catalog using additional temporary recording stations and refined detection methods. An analysis over the whole time period of the catalog may also improve the M_c.

4.2 Fault characterisation

To analyze the active faults in detail, we calculated 19 focal mechanisms using FOCMEC (Snoke 2003) for the master events of the detection periods in 2019 and 2020 (Fig. 4). For the 2018 detection periods in February 2018 and October 2018, Mader et al. (2021) already determined nine focal mechanisms of the strongest events. To image the active fault plane, we calculated relative hypocenter relocations with HypoDD (Waldhauser and Ellsworth 2000) for each detection periods with at least ten earthquakes (Figs. 4, 5, 6, Table 1). The dominant mechanism of the events is strike-slip faulting and only a minor number of events show oblique or

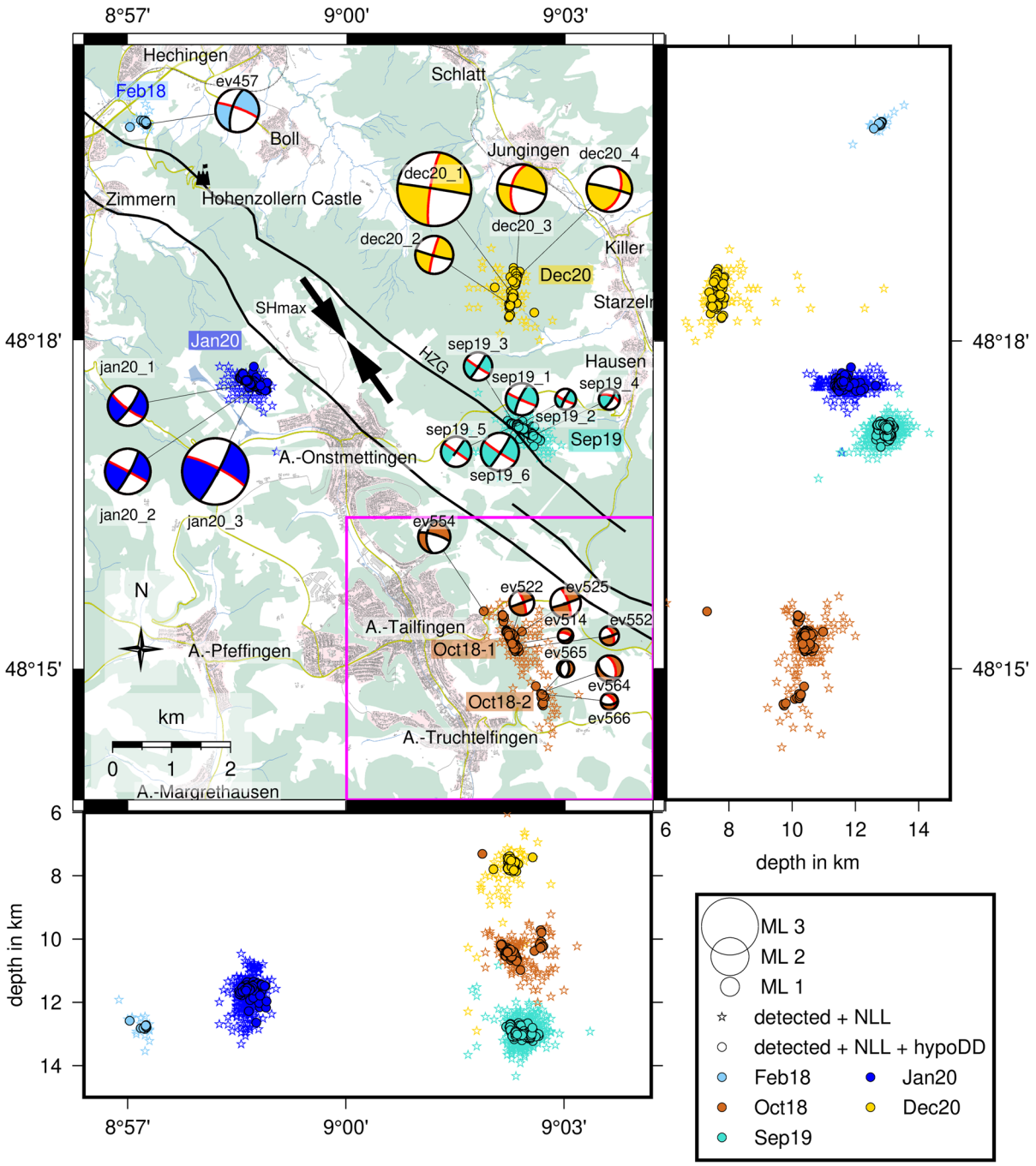

Fig. 6 HypoDD (circles) and NonLinLoc (stars, uncertainty < 2 km and at least 6 phase picks) hypocenter locations of the earthquake sequences Feb18, Oct18, Sep19, Jan20, and Dec20 and corresponding fault-plane solutions (Feb18 and Oct18 fault-plane solutions after Mader et al. (2021)). If known, the active fault plane is colored in red. Black lines indicate boundary faults of the Hohenzollerngraben (HZG, Regierungspräsidium Freiburg: Landesamt für Geologie, Rohstoffe und Bergbau (Hrsg.) 2019) and the black arrows show the direction of $S_{H_{max}}$ after Mader et al. (2021). The sizes of the fault-plane solutions are scaled with magnitude. The magenta frame borders the close-up area of Fig. 8. Background map created with OpenStreetMap Data (2022, downloaded via geofabrik.de)

normal faulting (Fig. 4, Table 3). The relative hypocenter relocations allow to identify the fault planes due to the improved precision compared with the absolute hypocenter locations of the LED (Fig. 23).

4.2.1 NNE-SSW striking fault planes

We observe two event sequences in November and December 2020 (Nov20 and Dec20), for which relative hypocenter relocations are located at 5 - 10 km depths and indicate a nearly NNE-SSW striking, steeply dipping fault plane (Figs. 4, 6, 7, 20, and 21). Together with the corresponding fault-plane solutions, we identify the sinistral strike-slip motion as source mechanism (Figs. 4, 6, and 7). The Dec20 sequence is located between the towns Albstadt-Onstmettingen and Jungingen, just north of the HZG in an area of continuous seismic activity. The Nov20 sequence is located about 6 km south of the town Meßstetten, about 20 km south of the HZG, in an area of reduced seismic activity (Fig. 4).

4.2.2 NW-SE striking fault planes

The relative hypocenter relocations of earthquake sequences in February 2018, September 2019 and January 2020 (Feb18, Sep19, Jan20) outline steeply dipping NW-SE oriented fault planes, which are nearly parallel to the strike of the HZG (Figs. 6 and 7). This is in good agreement with the dextral fault plane of the strike-slip focal mechanisms. The depth range of the three earthquake sequences is 11 - 15 km. The Feb18 and Sep19 sequences are located below the northeastern HZG boundary fault, with the Feb18 sequence close to the Hohenzollern Castle and the Sep19 sequence between the towns Albstadt-Onstmettingen and Hausen i. K.. The Jan20 sequence is located just south of the southwestern HZG boundary fault, NW of Albstadt-Onstmettingen.

4.2.3 NNW-SSE striking fault planes

During the event series from October to November 2018, we observe two separate earthquake sequences south of the HZG just east of Albstadt-Tailfingen and Albstadt-Truchtelfingen (Figs. 6, 7, and 8). The first earthquake sequence started on 15 October 2018 and lasted until end of October 2018 (Oct18-1, Fig. 9). The second, a smaller sub-sequence, occurred at the end of November 2018 (Oct18-2, Fig. 9). We first interpreted those two sequences as one sequence due to the temporal and spacial proximity. The analysis of all events with a similarity matrix highlights a slight difference in waveforms between the events in October 2018 (Oct18-1) and November 2018 (Oct18-2) (Fig. 24). This observation is also supported by fault-plane solutions determined by Mader et al. (2021), indicating a change from dominantly strike-slip in October 2018 to normal faulting in November 2018 (Fig. 6). Also, relative hypocenter relocations indicate a clear NNW-SSE striking fault plane for the Oct18-1 earthquake sequence, which corresponds to the sinistral strike-slip nodal plane of the focal mechanisms (Figs. 6 and 7). The relative hypocenter relocations of Oct18-2 are located about 1 km to the south of Oct18-1 (Figs. 6 and 8). Both sequences image a fault plane dipping towards the NE (Fig. 7). The depth range of the two sequences is 9 - 12 km with the Oct18-1 sequence located deeper than Oct18-2 sequence (Fig. 6).

5 Discussion

5.1 Characterisation of earthquake sequences

Earthquakes in the Swabian Jura are mostly related to single earthquakes and main-shocks with fore- and aftershock sequences, whereas the observation of earthquake swarms has so far not been described (e.g. Haessler et al. 1980, Mader et al. 2021, Stange and Brüstle 2005, Turnovsky 1981). This may be the case, as most analyses regarding the earthquakes in the area of the ASZ focused on the analysis of main shocks and their aftershocks. After Mogi (1963), we consider a sequence as earthquake swarm, if we observe a more gradual increase and decrease of event occurrences with time, without a clear main shock. Earthquake swarms are considered to be triggered by the propagation of fluids and the related pore pressure change (Hainzl 2004, Hainzl and Ogata 2005). As another possible driving force for earthquake swarms, especially on transform faults, shallow aseismic creep was identified (Lohman and McGuire 2007, Roland and McGuire 2009).

Globally, a b-value of 1 is observed in tectonic regions (El-Isa and Eaton 2014, Frohlich and Davis 1993). A temporal deviation of the b-value from 1 in a tectonic region may indicate a change of the stress

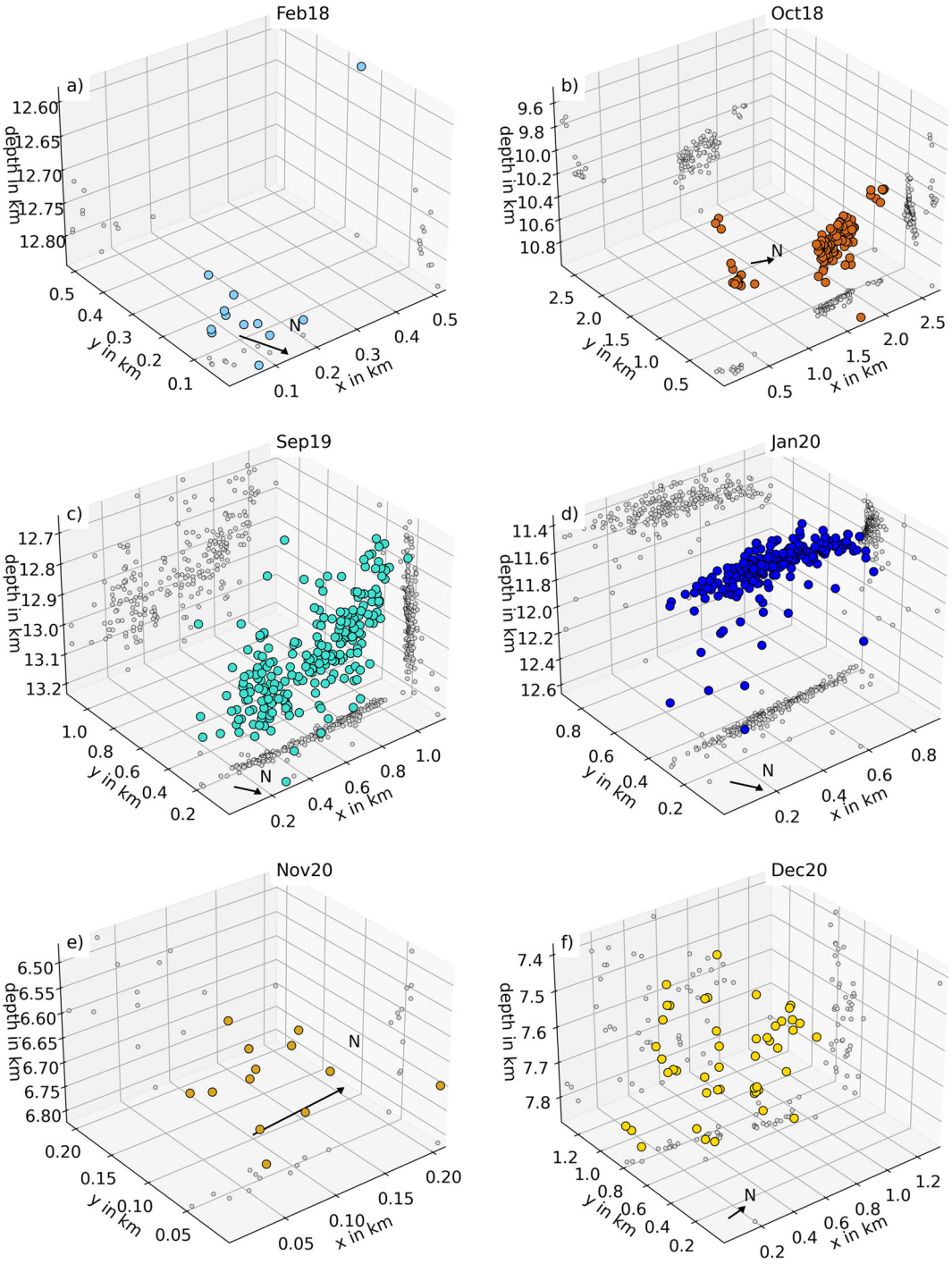

Fig. 7 3-D representation of HypoDD earthquake relocation hypocenters of all earthquake sequences: a) Feb18, b) Oct18, c) Sep19, d) Jan20, e) Nov20, f) Dec20 rotated along the strike direction of the fault plane (colored circles). Grey circles show projections of the hypocenter locations to the xy-, xz- and yz-plane to illustrate the spatial extension of the sequences. The black arrows indicate the north direction

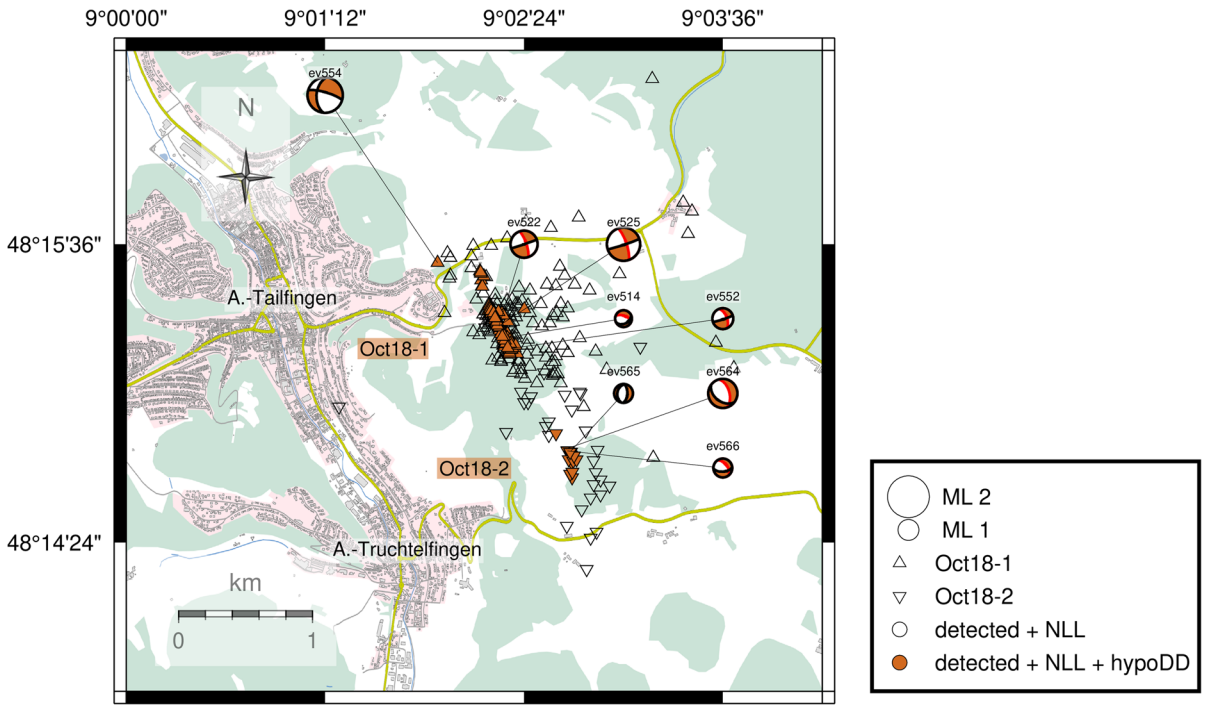

Fig. 8 Close-up view of the Oct18 earthquake sequences. The filled symbols represent the relative hypocenter relocations, unfilled symbols represent the NLL hypocenter locations. The triangles represent all events during the main activity in October 2018 (Oct18-1), whereas the inverted triangles represent the hypocenters of events during the second sub-sequence in November 2018 (Oct18-2). A clear temporal and spatial separation of the Oct18-1 and Oct18-2 sequence is visible

field on the fault system due to, for example the occurrence of an earthquake or a change in pore pressure (El-Isa and Eaton 2014). Varying b-values have been observed for different occasions like before and after major earthquakes, as well as for earthquake swarms (El-Isa and Eaton 2014).

We determine the b-value for the earthquake sequences (Fig. 9). We here analyze only our largest earthquake sequences Oct18, Sep19, Jan20 and Dec20, as the number of events within the other sequences is too small for a meaningful analysis. The determined b-values of three sequences are close to 1 (± 0.2, Oct18, Sep19, Jan20), which is the typical b-value observed in tectonic regions (Fig. 9a, c, e , Frohlich and Davis 1993, Mogi 1962). For the fourth sequence (Dec20), we observe a relatively small b-value of 0.46 (Fig. 9g).

The main activity of the Jan20 sequence is focused during two days and the strongest event has a magnitude *ML* of 3.5, which is more than one magnitude stronger than the second strongest event with *ML* 2.4 of the sequence (Figs. 9e, f). For this reason we identify the *ML* 3.5 earthquake as main shock of the Jan20 earthquake sequence. The corresponding b-value is 0.82. We classify the Jan20 earthquake sequence as an fore- and aftershock sequence, as we can clearly identify the main shock. Here, clearly more foreshocks (287) than aftershocks (61) are observed, which is mostly observed the other way round (Mogi 1963).

For the Dec20 earthquake sequence the *ML* 3.9 earthquake on 1 December 2020 could be identified as main shock (Fig. 9g). It is 1.3 magnitude units stronger than the second strongest observed event. The b-value is quite low with 0.46. This may be the result of the smaller amount of observed earthquakes, which also makes it difficult to identify the magnitude of completeness M_c. Another explanation may be non-Poissonian distributed seismicity within a fore- and aftershock sequence.

The strongest event during the main activity of the Oct18-1 earthquake sequence is the magnitude 1.7

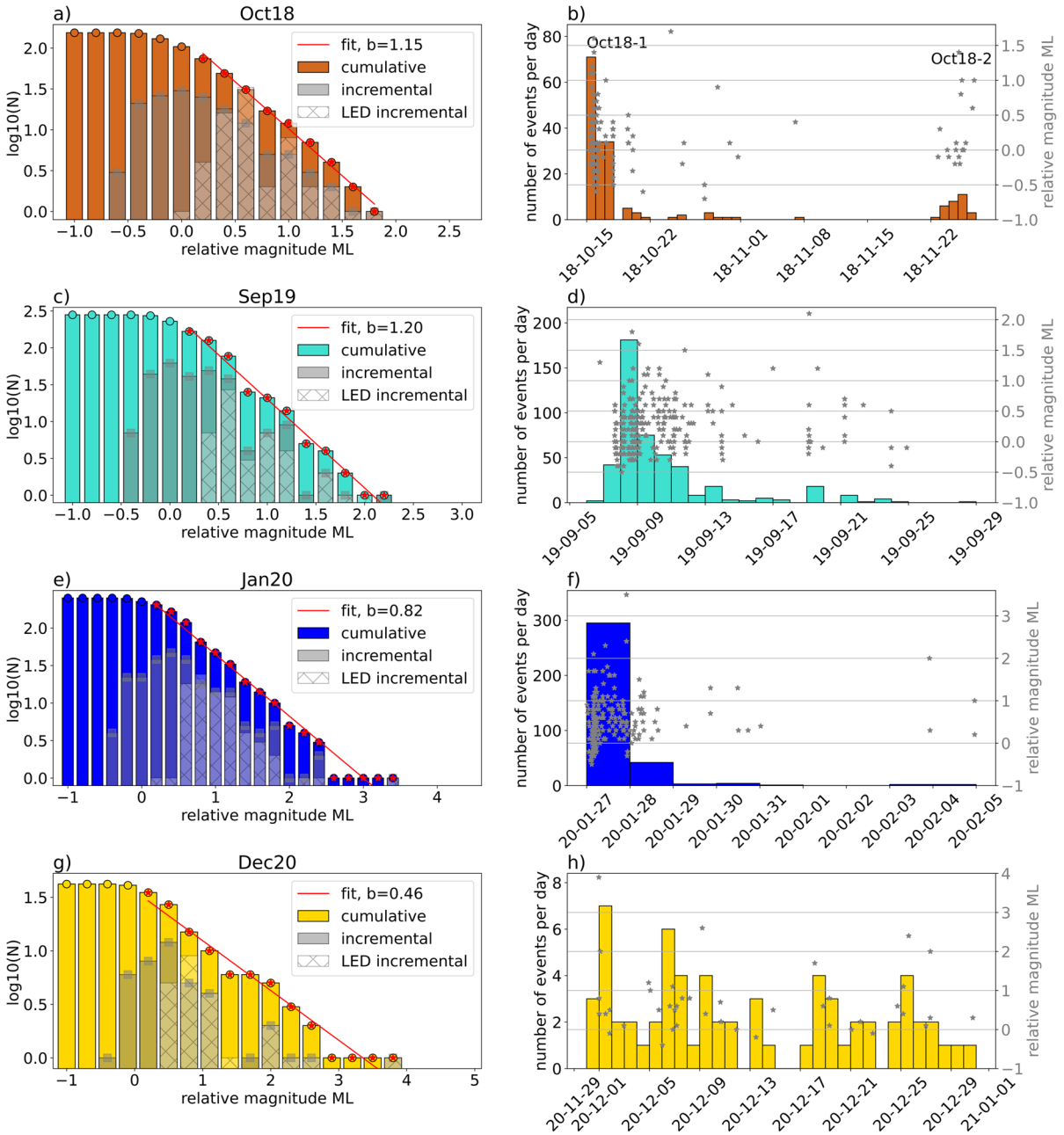

Fig. 9 Magnitude-frequency distributions in comparison with the LED magnitudes of the largest earthquake sequences (Oct18, Sep19, Jan20, Dec20, a,c,e,g). Red lines give the b-value fit of the magnitude-frequency distribution of the earthquake sequences, determined using least squares fitting. The assumed M_c for the b-value fit was 0.2, the bin width of the magnitude-frequency distribution is 0.2 magnitudes or 0.4 magnitudes in case of Dec20 due to the lesser number of events within the earthquake sequence. Temporal distributions of the events (b,d,f,h) of the largest earthquake sequences (Oct18, Sep19, Jan20, Dec20). The bars of the histogram show the number of earthquakes per day and the stars represent the earthquakes relative magnitudes. Based on their relative magnitudes and temporal distribution Oct18 and Sep19 are considered swarm-like earthquake sequences, whereas Jan20 and Dec20 show a clear main-shock on the 27 January 2020 and 1 December 2020, respectively.

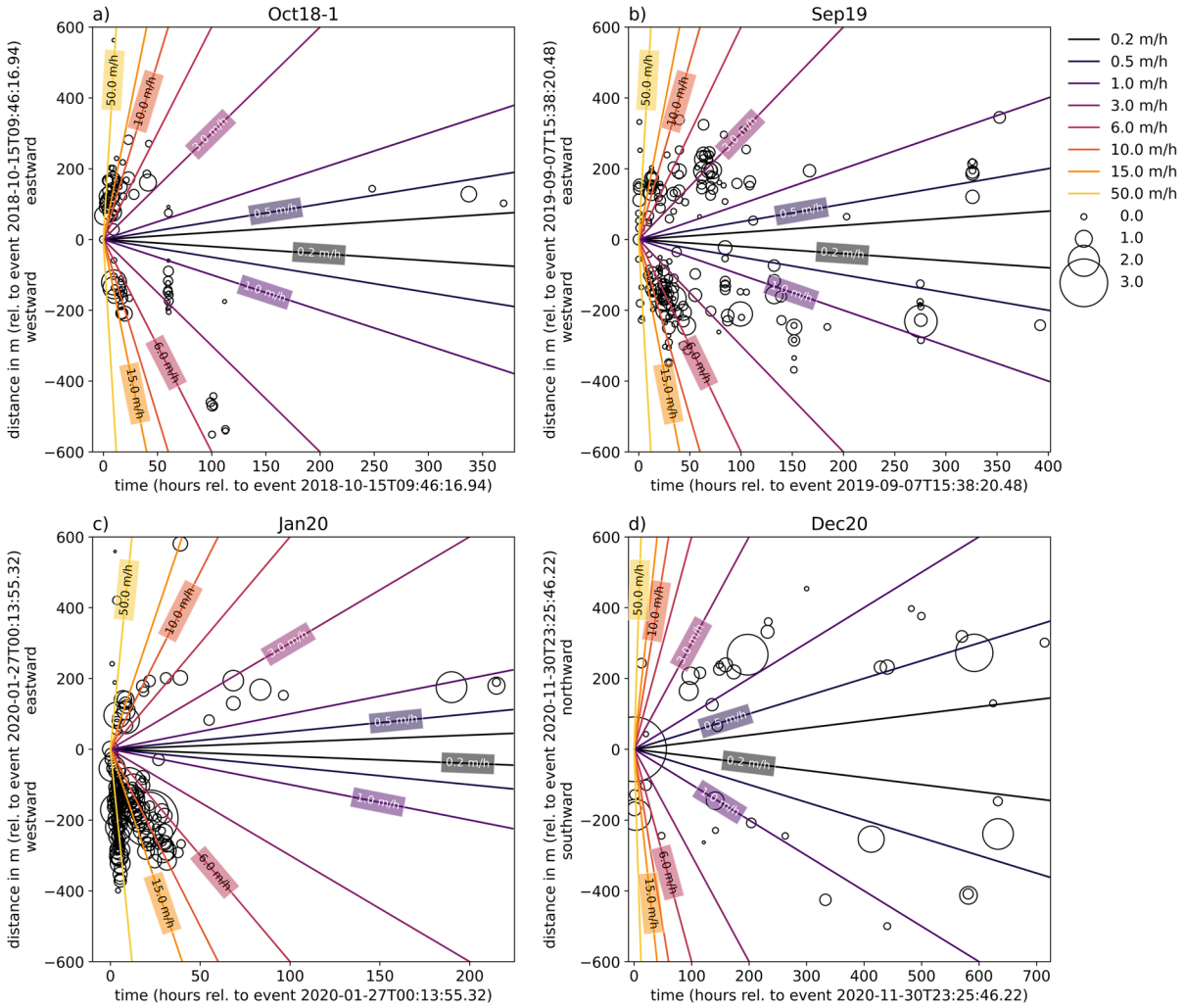

Fig. 10 Temporal and spatial migration along the faults relative to the first occurring event within the earthquake sequences a) Oct18-1, b) Sep19-1, c) Jan20, d) Dec20. The circles are scaled with magnitude and the lines indicate the apparent migration velocities.

earthquake on 24.10.2018 (Fig. 9a, b). The magnitude difference to other events is only 0.1 magnitude units, which is within the uncertainty range of ±0.2 of the magnitude estimation, so a clear main shock cannot be identified. The temporal distribution of the Oct18-1 sequence exhibits similarity to a fore- and aftershock sequence. Nevertheless, we classify the Oct18-1 sequence as a swarm-like activity due to the lack of a clearly identifiable main shock (Fig. 9a, b, Mogi 1963).

The Oct18-2 earthquake sequence has also a swarm-like activity. Here, also the identification of a clear main shock is difficult (magnitude difference of 0.4 magnitudes) and the temporal distribution is more gradual like expected for an earthquake swarm (Fig. 9b, Mogi 1963).

We also clearly observe a gradual increase and decrease of event occurrences with time during the Sep19 earthquake sequence, which is typical for an earthquake swarm (Fig. 9d, Mogi 1963). The strongest events of the Sep19 sequence have magnitudes of 2.1, 1.8 and 1.6. As we do not observe a magnitude difference larger than 0.3 between the strongest events and we observe no typical fore- and aftershock sequence distribution, a main shock is difficult to identify. For this reason, we consider the Sep19 earthquake sequence to be an earthquake swarm.

Both swarm-like sequences (Oct18, Sep19) have a b-value close to or greater 1, whereas the fore- and aftershock sequences (Jan20, Dec20) show reduced b-values. For earthquake swarms in West Bohemia also b-values close to 1 where observed (Čermáková and Horálek 2015, Hainzl 2004) and as driving force a combination of fluid movement and stress triggering is suggested (Hainzl 2004, Hainzl and Ogata 2005).

5.2 Migration velocity

For all four sequences we observe varying temporal patterns. The HypoDD locations and origin times can be used to estimate the migration velocity of the hypocenters within the earthquake sequences (Fig. 10). After the fast initiation of the rupture with about 50 m/h of the sequence Oct18-1, it propagated bilaterally eastwards and westwards with a velocity of about $15 \pm 5\, m/h$ for about 20 hours (Fig. 10a). A similar rupture behaviour is observed for the other swarm-like earthquake sequence Sep19 with a somewhat lower migration velocity of about $3-10\, m/h$ (Fig. 10b). Both sequences (Oct18-1, Sep19) show the reoccurence of high migration velocity pulses after the first activity (Fig. 10b). In contrast, the Jan20 sequence is more unilateral with an increased activity towards west (Fig. 10c). The migration pattern shows two migration episodes, the first with a high migration velocity of about 50 m/h towards the west and a second migration including the main shock with a reduced migration velocity of about 10 m/h. The Dec20 earthquake sequence related with the ASZ is much more scattered in space and time (Fig. 10d). After the main shock, relatively few aftershocks occur and the events happen to the south and north for ca. 650 hours. Although, there is no clear spatial migration trend, the velocity of the rupture front is low with about 0.5-2 m/h. These low migration velocities ($< 10\, m/h$) could be due to a fluid diffusion process to trigger microseismicity (Dublanchet and De Barros 2021, Hainzl 2004, Shapiro and Dinske 2009). The Dec20 sequence could also be triggered by a Coulomb stress change after the main shock. The high migration velocity pulses of the other sequences, especially at the beginning (Oct18-1, Sep19, Jan20, Fig. 10a-c) seem to be related with an aseismic slip process (Bhattacharya and Viesca 2019, Dublanchet and De Barros 2021). Thus, the observed dual migration velocities may support the model by Dublanchet and De Barros (2021) with these sequences. Further analysis could help to identify possible driving mechanisms and highlight the differences of the observed earthquake sequences in more detail, which is beyond the scope of our study.

5.3 Fault characterisation

The analysis of the six earthquake sequences with more than 10 events (Feb18, Oct18, Sep19, Jan20, Nov20, Dec20) allows us to identify and image three different types of faults, which were seismically active in the Swabian Jura during 2018 to 2020 (Figs. 4, 6, and 11). Here, we are going to discuss our findings in context with the regional tectonics, the stress field and the tectonic model of the ASZ defined by Reinecker and Schneider (2002).

5.3.1 NNE-SSW striking fault planes

The first fault type observed in the Nov20 and Dec20 sequences is related to NNE-SSW striking sinistral strike-slip faulting in a depth range of 5 - 10 km in the crystalline basement(Fig. 4). This fault mechanism is consistent with the previously imaged orientation and kinematics of the ASZ (e.g. Haessler et al. 1980, Stange and Brüstle 2005, Turnovsky 1981). The Dec20 sequence is located between Jungingen and the northern graben boundary of the HZG in the area of continuous seismic activity (Figs. 4 and 6). The Nov20 sequence images the NNE-SSW striking fault plane south of Meßstetten. This seismically active fault segment is located about 20 km south of the HZG in an area of reduced seismic activity (Fig. 4). This observation suggests an extension of the seismically active area of the ASZ further to the south as proposed by Mader et al. (2021). The reduced seismicity in the area south of Meßstetten may result from either an aseismic creeping component or a seismic gap caused by a locked fault plane, which was partially activated during the Nov20 sequence. The observed fault planes in this area, which are related with the ASZ, cover a depth extension of maximum 10 km. From previous studies we know that the seismicity related with the ASZ is located even deeper in the upper crust (about 1 - 18 km depth, Mader et al. 2021). The limited depth range of

the here observed NNE-SSW sinistral strik-slip faults may be related with the short observation times of the two sequences from 2018 to 2020.

5.3.2 NW-SE striking fault planes

Second, we clearly observe dextral strike-slip faulting with a NW-SE strike, almost parallel to the HZG and epicentral locations close to the HZG boundary faults (Fig. 6, Feb18, Sep19, Jan20). This type of faulting was so far not directly observed in the area of the town Albstadt. Nevertheless, the stress inversion by Mader et al. (2021) already suggested the NW-SE striking fault plane of the event ev457 (Feb18 sequence, Fig. 6, Table 3) as the most probable active fault plane to rupture in the current stress regime. However, due to the general NS alignment of the seismicity in the area so far always the about NNE-SSW striking fault plane was expected to be the active one. The active faults of the Feb18, Sep19 and Jan20 earthquake sequences are located about parallel and close to the HZG boundary faults. We observe at least two vertically dipping faults outlined by the three sequences (Fig. 7), one close to the southwestern boundary fault and one along the northwestern boundary fault of the HZG (Fig. 6). All three sequences are located at depths of 11 - 15 km, which is significantly below the estimated depth extension of 2 - 3 km of the boundary faults of the HZG (Illies 1982, Schädel 1976). A continuation of the HZG to greater depth is debated but not proven yet, as no analysis could so far image a depth extension of the HZG into the crystalline basement (Illies 1982, Schädel 1976). Illies (1982) suggests a continuation of the northeastern boundary fault of the HZG into the crystalline basement, based on the differences in the characteristics of the outcropping boundary faults, gravity measurements and the hypocenter distribution. This depth continuation would result in a Y-shaped pattern of the HZG faults, with the HZG boundary faults converging in 2 - 3 km depth and a continuation of the northeastern boundary fault towards greater depth. We suggest that our identified faults are not directly connected to the HZG as we observe at least two steeply dipping fault planes, which would correspond to a X-shaped continuation of the graben structure with depth. Instead, we propose an inherited zone of weakness or fault zone in the area below the HZG, which may facilitate the rupture origin of the observed earthquakes and may also have facilitated the development of the HZG in this particular area. The depth and strike of a structural element, which is actually reactivated in the present stress field, depend on the pre-existing structures or structural weaknesses. The here observed NW-SE striking deep structure can be imprinted from either Variscan basement processes (Echtler and Chauvet 1992, Hann et al. 2003) or Triassic and Palaeogene normal faulting (Reicherter et al. 2008) which partly strike NW-SE. This normal to transtensional faulting is found, e.g. in the en-echelon arranged graben structures, like the HZG or near the western Lake Constance and Hegau (Fig. 1). Thus, the earthquake sequences Feb18, Sep19, and Jan20 may be due to an activation of pre-existing faults in the upper crust induced by the present stress field ($S_{Hmax} \sim 149°$, Mader et al. 2021) as proposed by Reicherter et al. (2008). This rupture mechanism is supported by the results of Mader et al. (2021) and Röckel et al. (2022), who suggest that fault planes with NW-SE and NNE-SSW strike are favorably aligned for rupture in the NNW-SSE directed maximum horizontal stress (Fig. 6). The activation of NW-SE oriented faults is also observed in the current stress field for example in the area of the Hegau-Bodensee Graben along the Freiburg-Bonndorf-Bodensee Fault Zone (FBBFZ, Fig. 1, Diehl et al. 2023). The eastern part of this fault zone is the western Lake Constance and Hegau south of the ASZ. There, also dextral strike-slip to transtensional faulting is observed with the faults striking parallel to the HZG (Diehl et al. 2023).

5.3.3 NNW-SSE striking fault plane

The Oct18-1 earthquake sequence is located in the area of major seismic activity of the ASZ near Albstadt and close to the southern boundary fault of the HZG (Fig. 6). The sinistral strike-slip fault plane strikes NNW-SSE and is therefore rotated counter-clockwise ($\sim 50°$) relative to the typical NNE-SSW fault orientation of the ASZ (Fig. 11, e.g. Haessler et al. 1980, Stange and Brüstle 2005, Turnovsky 1981) and it is also rotated clockwise ($\sim 40°$) relative to the newly observed NW-SE striking fault planes. The Oct18-2 sequence is offset from the Oct18-1 sequence by about 1 km to the southeast and the fault-plane solution points to a normal faulting mechanism, clearly different from the known strike-slip mechanisms of the ASZ (e.g. Haessler et al. 1980, Stange and Brüstle 2005, Turnovsky 1981). Both

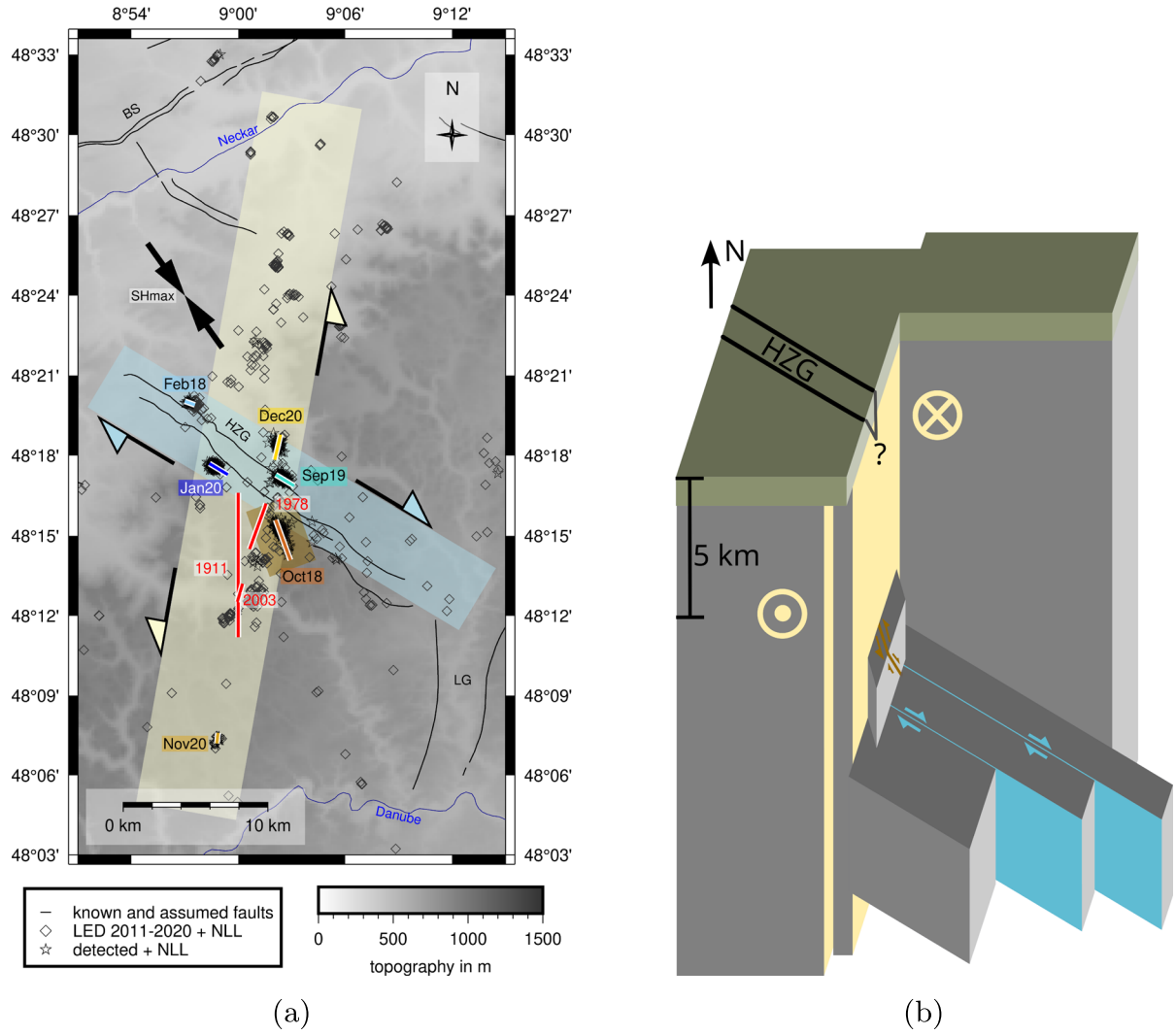

Fig. 11 a) Revised model of the Swabian Jura around Albstadt as derived in this study. Colored lines indicated active faults of earthquake sequences. Length is based on HypoDD hypocenter distribution. Red lines show rupture planes of the 1978 and 2003 earthquakes (after Stange and Brüstle 2005) and estimated rupter plane of the 1911 earthquake (after Schneider 1979, Wells and Coppersmith 1994). Blue (NW-SE dextral strike-slip) and yellow (ASZ) shaded areas represent the two active fault zones in the Swabian Jura. Colored arrows indicated the movement of the strike-slip faults and the black arrows show the direction of $S_{H_{max}}$ after Mader et al. (2021). Stars indicate reliable NonLinLoc locations (uncertainty < 2 km and at least 6 phase picks) of detected events. Squares indicate best located events in period 2011 to 2018 of Mader et al. (2021) complemented with newly located events in 2019 to 2020 using the ASZmod1 and station corrections in NonLinLoc (Mader et al. 2021). Topography is based on SRTM15+ (Tozer et al. 2019). b) Simplified, schematic 3-D model of the tectonic blocks at the ASZ. Blue (NW-SE dextral strike-slip) and yellow (ASZ) shaded areas represent the two major active fault zones like in a. The area of intersection between these two fault zones causes complex faulting as indicated by the dark-brown fault zone (Oct18-1 and Oct18-2 earthquake sequences). Arrows indicate the strike-slip movement. The greenish colored layer represents the sedimentary cover rocks, the gray colored blocks the crystalline basement of the upper crust. The model of Reinecker and Schneider (2002) consisted only of the ASZ (N-S striking sinistral strike-slip, yellow) and the en-echelon arranged graben structures in the cap rock above the ASZ

sequences, Oct18-1 and Oct18-2, are located in a depth range of 9 - 12 km, which places them above the 11 - 15 km deep NW-SE striking fault planes about parallel to the HZG and below the NNE-SSW striking fault plane of the ASZ observed here. The different rupture mechanism, including a normal faulting component, of the Oct18-1 and Oct18-2 sequences may be interpreted as a local stress perturbation caused by the intersection of the NNE-SSW striking ASZ (yellow colored events in Fig. 6) and the deeper NW-SE (blue colored events in Fig. 6) oriented inherited zone of weakness.

5.4 Seismically active faults in the area of the ASZ

The analysis of the earthquake sequences in the years 2018 to 2020 reveals a complex faulting structure below the Swabian Jura close to the town Albstadt (Fig. 11). The tectonic model for the area of Albstadt described by Reinecker and Schneider (2002) connects the two known tectonic structures, namley the HZG and the ASZ. In this model the sinistral strike-slip movement of the ASZ facilitates the opening of en-echelon arranged graben structures, like the HZG, in the cap rocks along the ASZ (Fig. 11, Reinecker and Schneider 2002, Tron and Brun 1991). Here, we suggest an addition to the tectonic model of Reinecker and Schneider (2002) in the form of an about NW-SE striking dextral strike-slip fault system below the HZG in about 11 - 15 km depth, also located in the upper crust (Fig. 11, blue color, Aichroth et al. 1992, Gajewski and Prodehl 1985). A straight connection between the HZG and the NW-SE striking faults cannot be resolved because of the differences in depth between the observed seismically active faults and the depth projection of the boundary faults of the HZG (Illies 1982, Schädel 1976). However, the existence of the NW-SE striking fault system could have enabled the formation of the HZG at its location. At the intersection of the NNE-SSW striking ASZ and the NW-SE striking fault system, we suggest a complex deformation zone, which was active during the Oct18-1 and Oct18-2 earthquake sequences. One explanation for the observed faulting may be bending along the NW-SE fault formed due to the overlap of the two fault systems. Another explanation may be a local deviation of the stress field due to the intersection of the two fault zones, inducing faulting along not preferentially aligned faults within the current regional stress field. Both, the ASZ and the NW-SE striking fault zone are aligned preferentially for activation in the current local stress field (Heidbach et al. 2016, Mader et al. 2021, Röckel et al. 2022). The driving force of the seismicity of both fault systems is therefore likely the Alpine orogeny, which influences the local stress field in the northern Alpine foreland (Kastrup et al. 2004, Mader et al. 2021, Singer et al. 2014). The intersection of the two fault systems may also facilitate the occurrence of the seismicity in the Swabian Jura, as it may act as stress concentrator (Fonsêca et al. 2021, Talwani 1988). Due to the limited study period of three years, further analysis is necessary to better verify or modify our proposed faulting model of the Albstadt region. Based on the current observations a segmentation of the ASZ cannot be verified nor denied. The same holds for the NW-SE fault zone, though here we observe at least two active faults. Further analysis could focus on resolving those faults with HypoDD relocations of more events over a longer time period. Such an improved model of the faulting styles and the possible maximum extensions of the involved faulting segments could also help to better determine the seismic hazard potential and prepare for future ground shaking. An earthquake rupturing the ASZ between the cities Jungingen and Albstadt-Ebingen for example could result in a magnitude similar to the *ML* 6.1 earthquake 1911 which caused major damage (Figs. 2, 11a, Schneider 1979, Schwarz et al. 2019, Wells and Coppersmith 1994).

6 Conclusion

We analyzed 12 detection periods with earthquakes in the area of the Swabian Jura using a multi-station template-matching approach. This procedure allows us to complement the official LED catalog with 1070 additional earthquakes, 592 of which are well located. Furthermore, we determine a relative event magnitude for 489 earthquakes, with the smallest event magnitude being -0.6. The observed earthquake sequences can be separated into fore- and aftershock sequences as well as earthquake swarms. The later type was so far not observed in the Swabian Jura. Relative hypocenter relocations and fault-plane solutions of the six major earthquake sequences allow us to image three different seismically active fault sets below the Swabian Jura near Albstadt. This complex fault structure consists not

only of the previously known NNE-SSW striking sinistral ASZ, but also NW-SE striking dextral fault planes parallel to the HZG and NNW-SSE striking sinistral fault planes with a normal faulting component. As a result, we introduce an extension to the tectonic model of Reinecker and Schneider (2002) in form of an additional NW-SE striking dextral fault zone at a depth of 11-15 km below the HZG. This fault zone is located within the crust, which acts as a zone of mechanical weakness and is activated by the regional tectonic stress field, which is likely dominated by geodynamic processes related to the Alpine orogeny. At the intersection of the newly identified NW-SE striking fault zone and the ASZ, rather complex faulting is observed. Due to the short time span of observation the depth range of the newly observed fault zones may change with future analyses. A direct connection of the HZG to the NW-SE striking dextral fault planes is unlikely as their depth ranges do not overlap. However, such NW-SE zones of weakness in the upper crust may assist the development of the NW-SE oriented shallow grabens in the region (Reinecker and Schneider 2002). The driving forces are likely related to stresses related to geodynamic processes of the Alpine orogeny and the faulting pattern is in good agreement with the one expected for the rollback model of Kissling and Schlunegger (2018). A downward bending of the European plate can well explain the shallow graben systems (e.g. FBBFZ and HZG). The migration velocities of our earthquake sequences may indicate, that fluids in the upper crust assist the rupturing.

Appendix A: Appendix

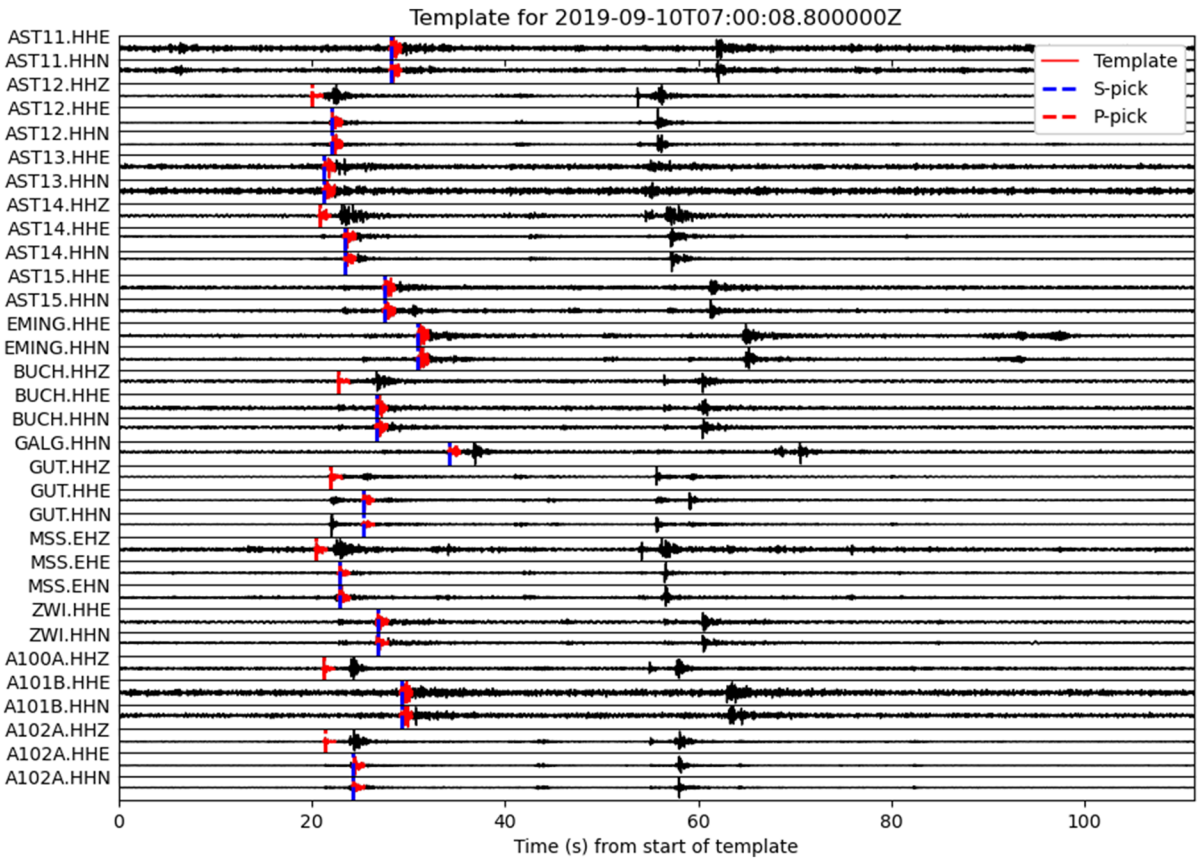

Fig. 12 Exemplary waveform template for a *ML* 1.1 earthquake on 10 September 2019 at 07:00

Table 6 Relationship between arrival time uncertainty and assigned quality based on Mader et al. (2021); ep represents the earliest possible pick and lp the latest possible pick

Phase arrival time uncertainties	lp-ep ≤ 0.05	$0.05 <$ lp-ep ≤ 0.1	$0.1 <$ lp-ep ≤ 0.2	$0.2 <$ lp-ep ≤ 0.4	lp-ep > 0.4
Quality	0	1	2	3	4

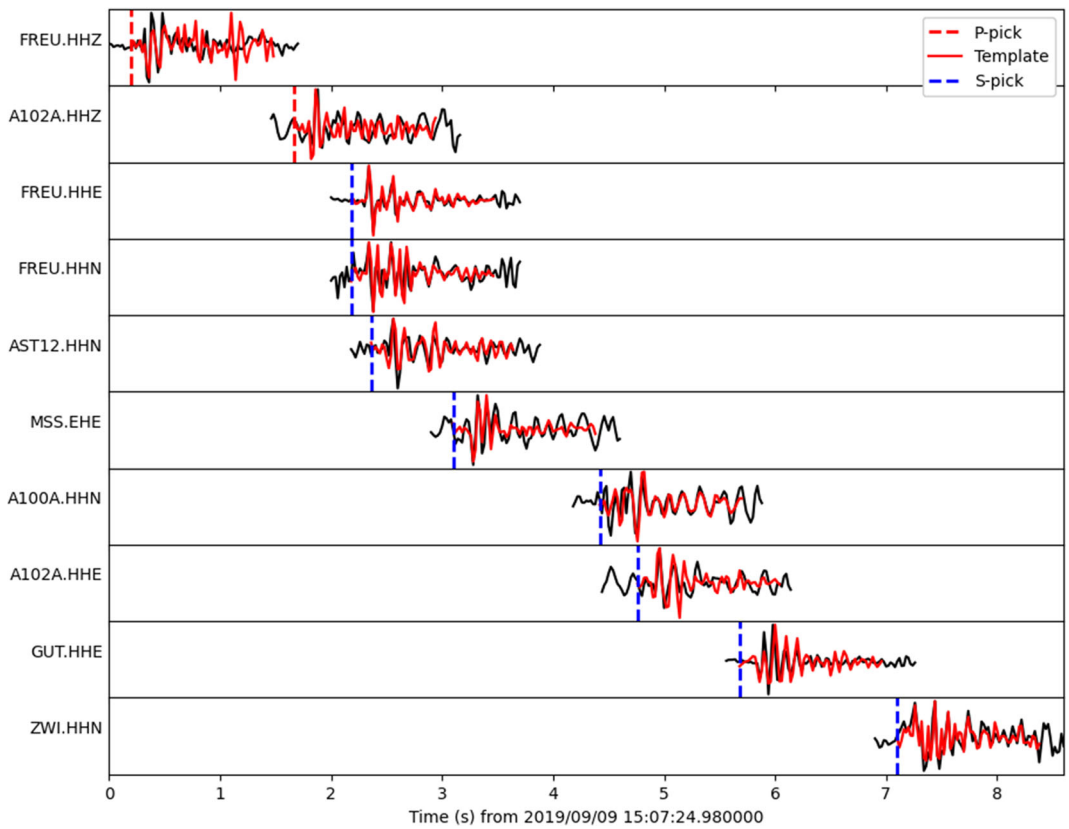

Fig. 13 Exemplary waveforms for a detected event on 9 September 2019 at around 15:00 and the corresponding automatically determined phase arrival times. Here, the phase arrival times are not yet corrected for the 0.15 s offset due to the prepick time of the waveform template

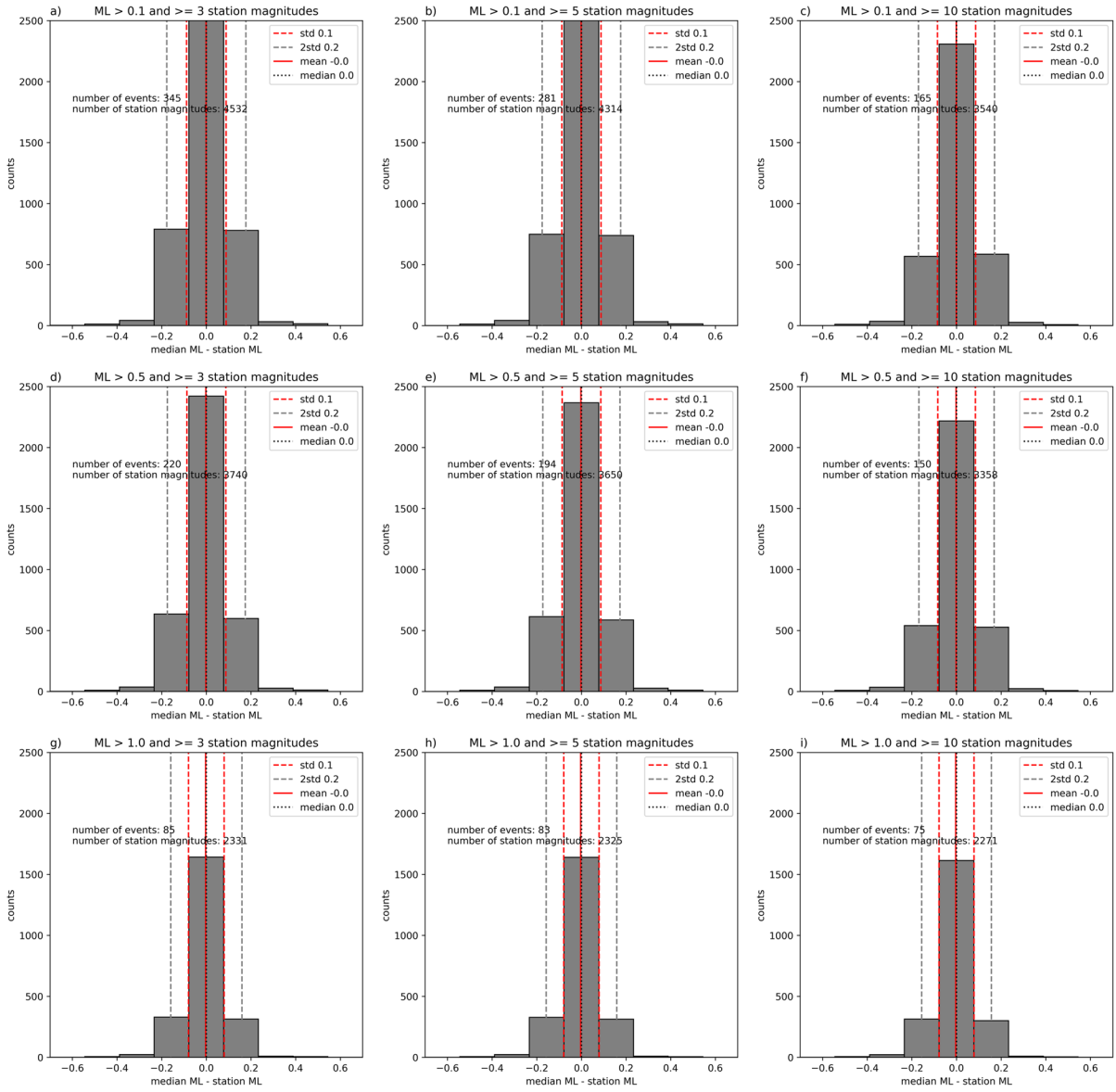

Fig. 14 Histograms of differences between median and station relative magnitude, for different subsets of all determined relative magnitudes (a-i), with different minimum magnitude and number of station magnitudes allowed. In the histogram data templates are excluded. For all subsets median, mean and standard deviation (std) are determined and have neglectable variations

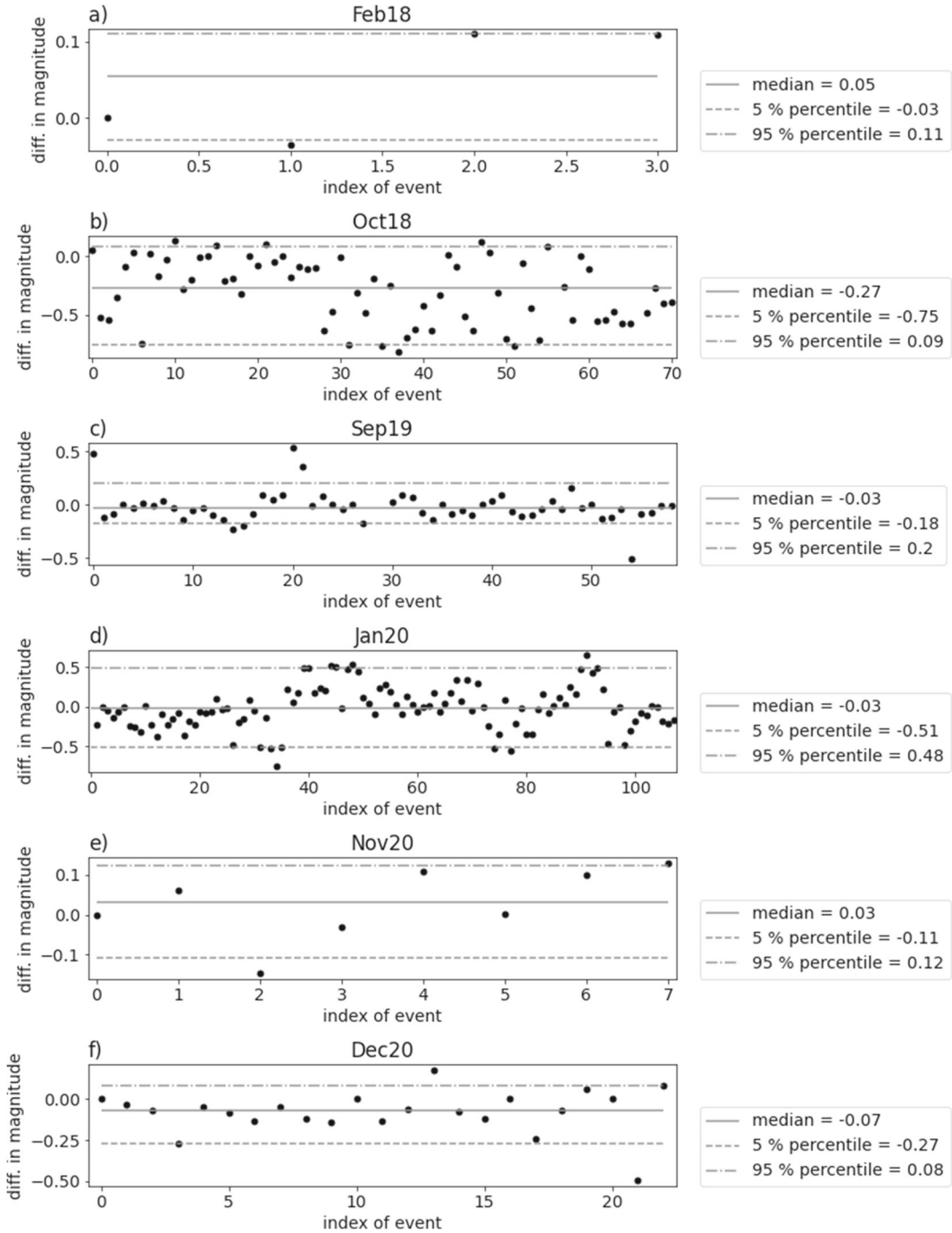

Fig. 15 Difference between our relative magnitude result and the magnitude determined by the LED (Bulletin-Files des Landeserdbebendienstes B-W 2011-2020) a) for Feb18, b) for Oct18, c) Sep19, d) Jan20, and e) Dec20 earthquake sequences. Gray lines indicate the median (solid), 5 % percentile (dashed) and 95 % percentile (dashdot) of the differences in magnitude

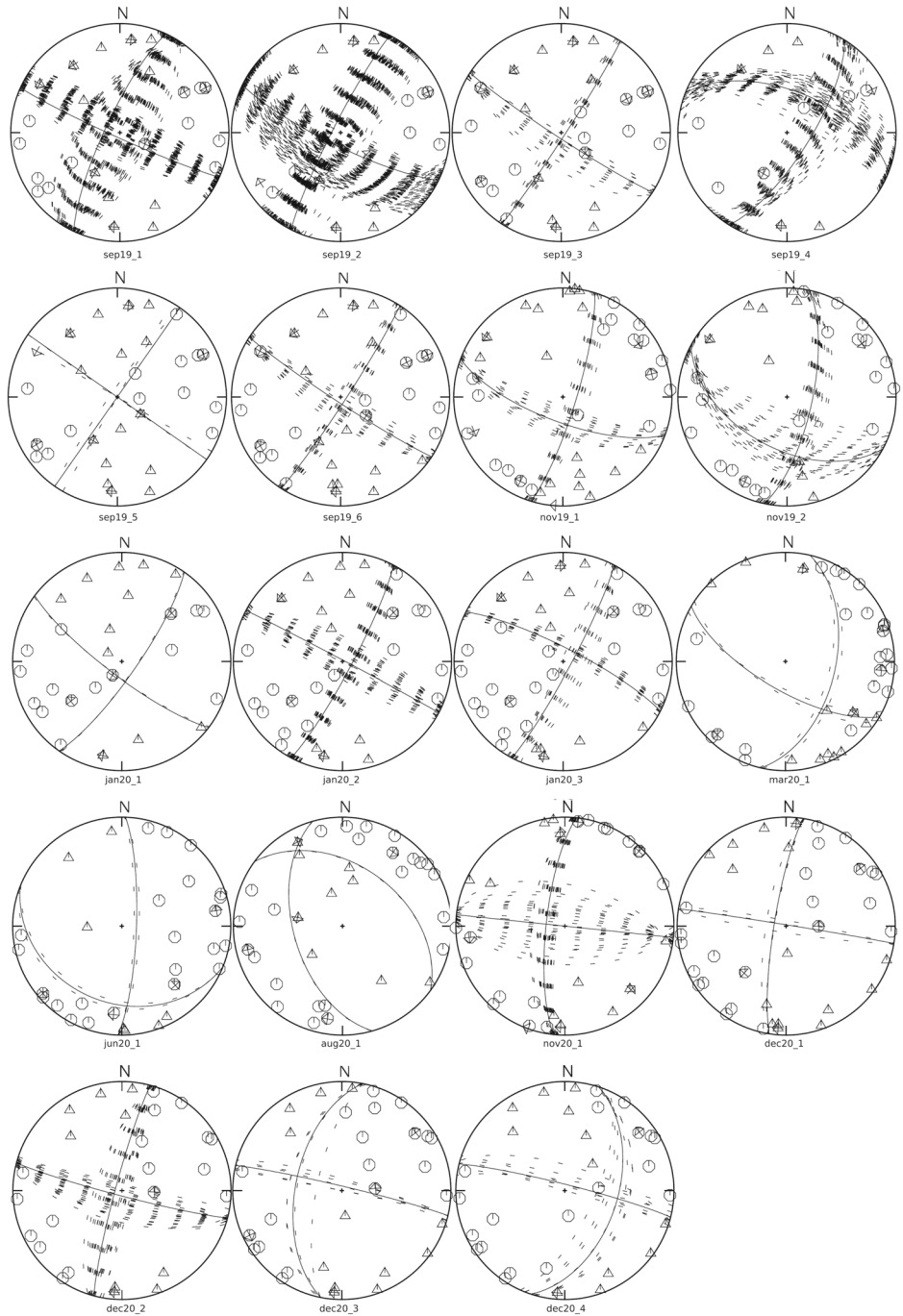

Fig. 16 Overview of calculated fault-plane solutions with preferred (solid line) and all possible solutions (dashed lines). Triangles are negative and hexagons are positive P-polarities. Arrows (mostly overlapping with other symbols) indicate direction of SH-polarity. Fault-plane solutions are labeled with their ID from Table 3

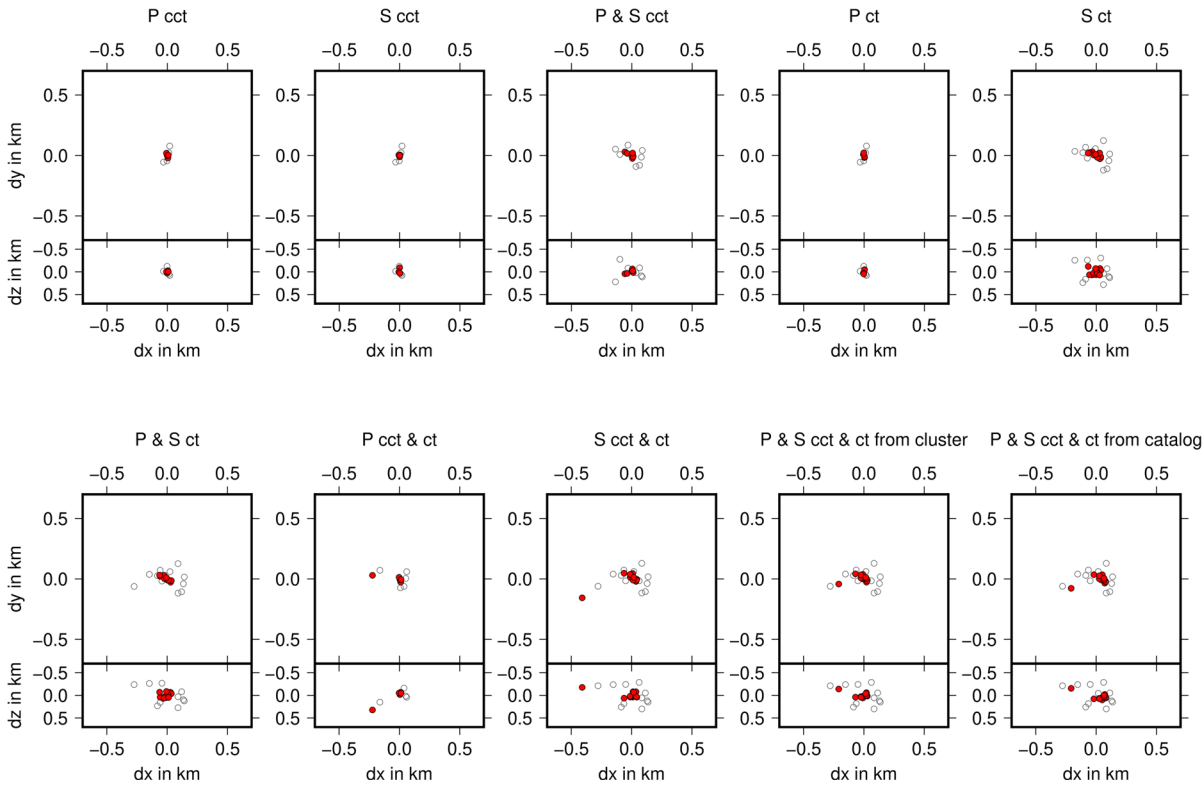

Fig. 17 Comparison of HypoDD performance with different data sets on the Feb18 earthquake sequence. Black circles represent NLLoc hypocenter locations. Red filled circles show result of HypoDD. Title represents data set used (ct=catalog times, cct=cross-correlation times, from cluster or catalog represents the inversion starting point)). Hypocenter locations are always displayed in map view and corresponding West-East depth slice below

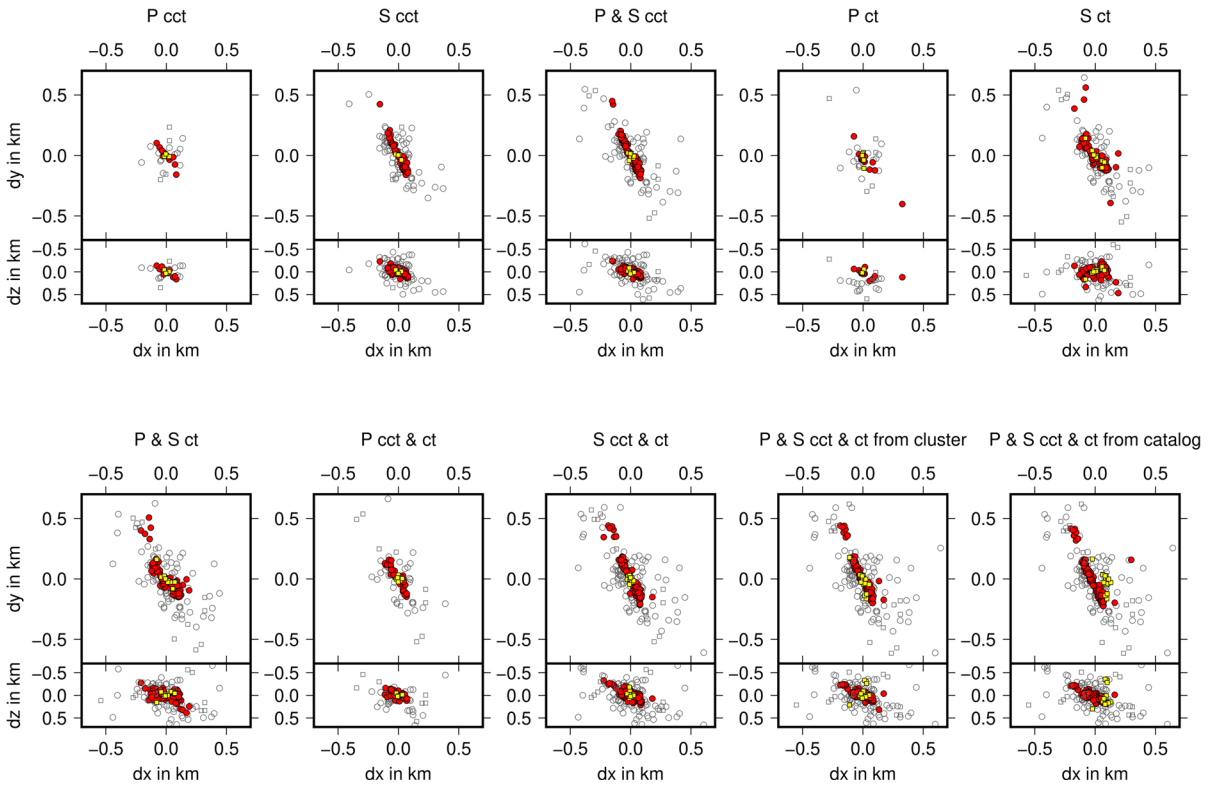

Fig. 18 Comparison of HypoDD performance with different data sets on the Oct18 earthquake sequence. The Oct18 sequence is separated in two clusters. Hypocenter location is always relative to cluster center. Black circles (Oct18-1) and squares (Oct18-2) represent NLLoc hypocenter locations. Red filled circles (Oct18-1) and yellow filled squares (Oct18-2) show the result of HypoDD. Title represents data set used (ct=catalog times, cct=cross-correlation times, from cluster or catalog represents the inversion starting point)). Hypocenter locations are always displayed in map view and corresponding West-East depth slice below

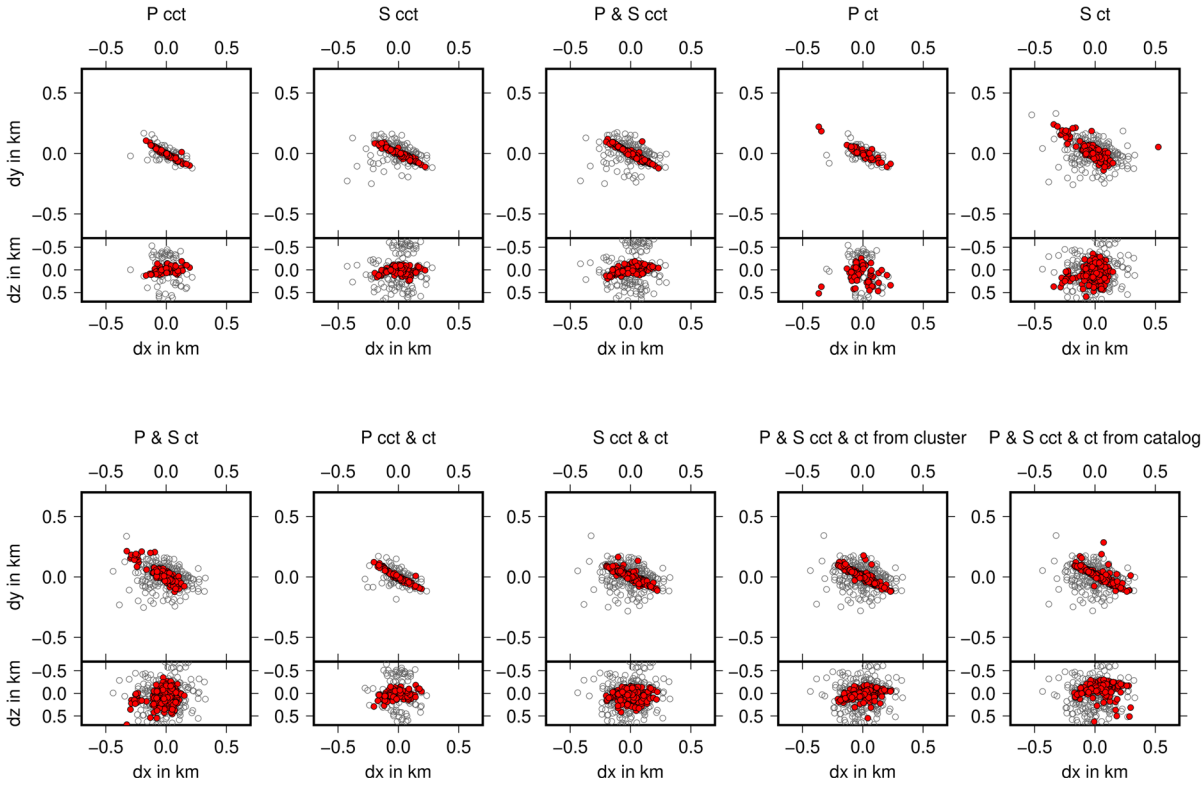

Fig. 19 Comparison of HypoDD performance with different data sets on the Jan20 earthquake sequence. Black circles represent NLLoc hypocenter locations. Red filled circles show result of HypoDD. Title represents data set used (ct=catalog times, cct=cross-correlation times, from cluster or catalog represents the inversion starting point)). Hypocenter locations are always displayed in map view and corresponding West-East depth slice below

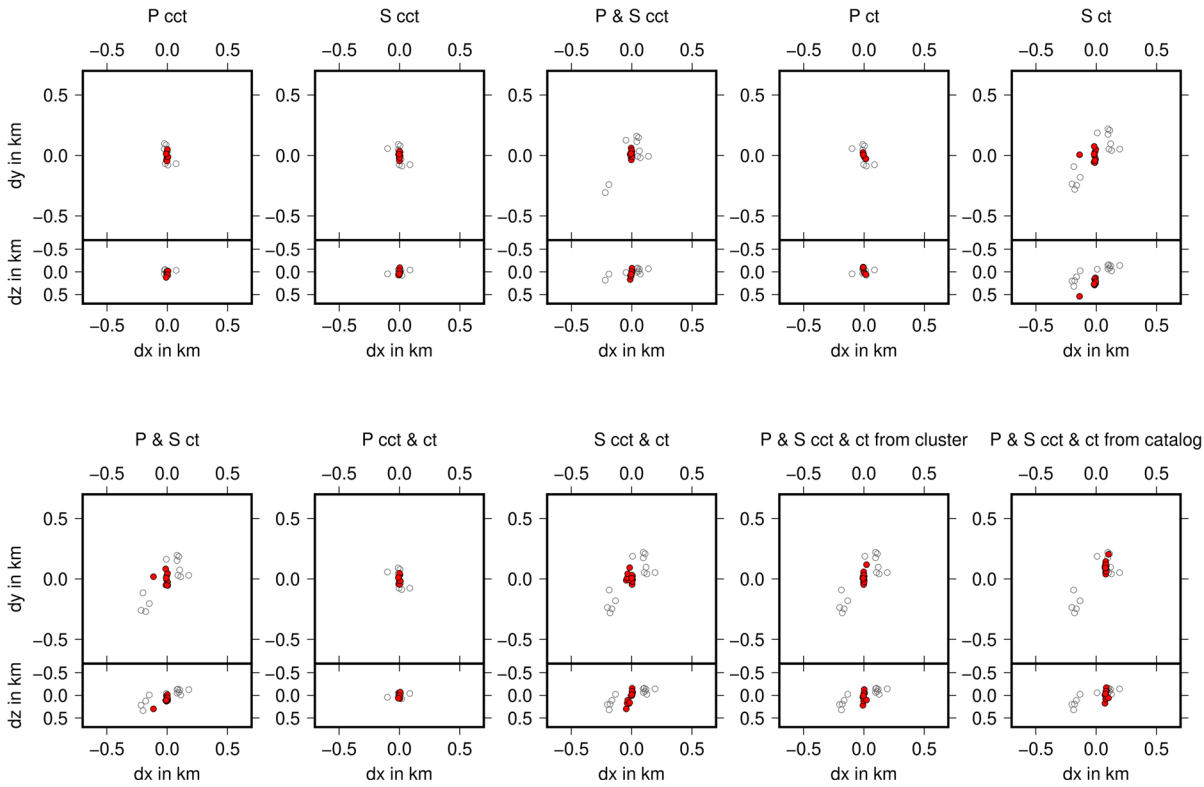

Fig. 20 Comparison of HypoDD performance with different data sets on the Nov20 earthquake sequence. Black circles represent NLLoc hypocenter locations. Red filled circles show result of HypoDD. Title represents data set used (ct=catalog times, cct=cross-correlation times, from cluster or catalog represents the inversion starting point)). Hypocenter locations are always displayed in map view and corresponding West-East depth slice below

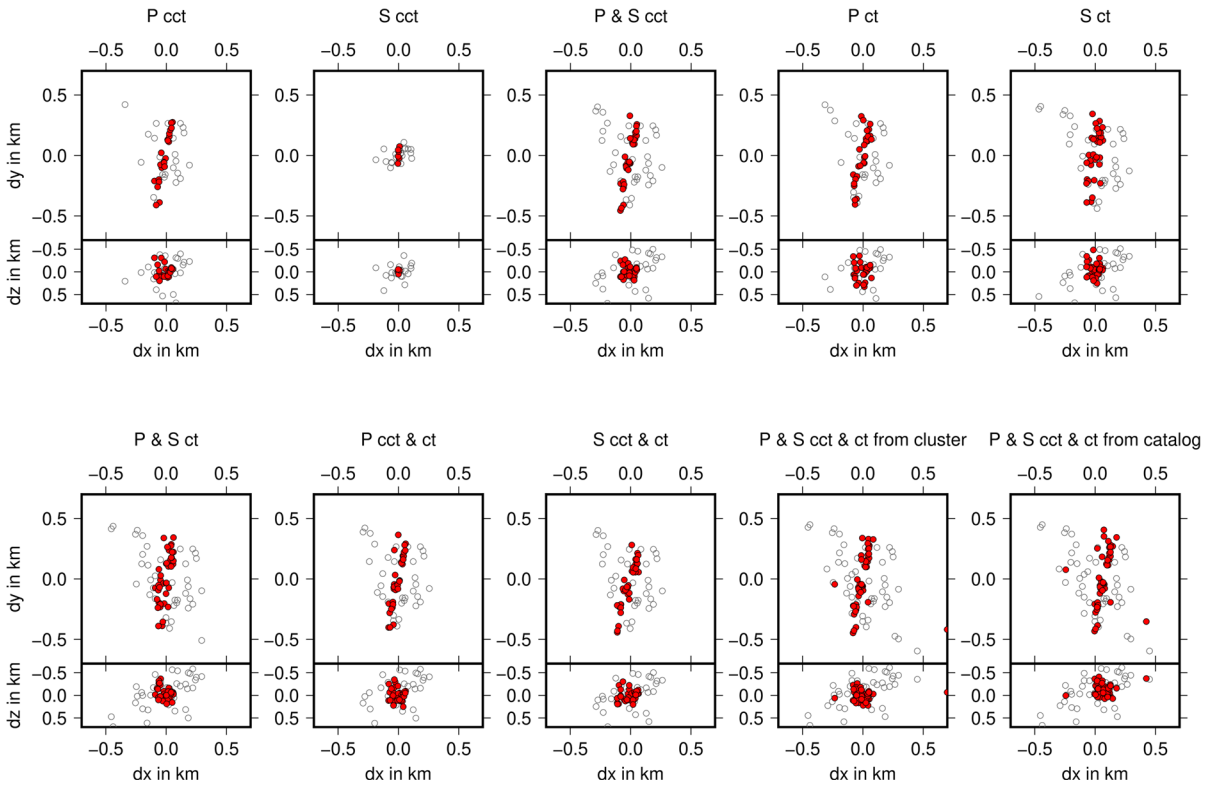

Fig. 21 Comparison of HypoDD performance with different data sets on the Dec20 earthquake sequence. Black circles represent NLLoc hypocenter locations. Red filled circles show result of HypoDD. Title represents data set used (ct=catalog times, cct=cross-correlation times, from cluster or catalog represents the inversion starting point)). Hypocenter locations are always displayed in map view and corresponding West-East depth slice below

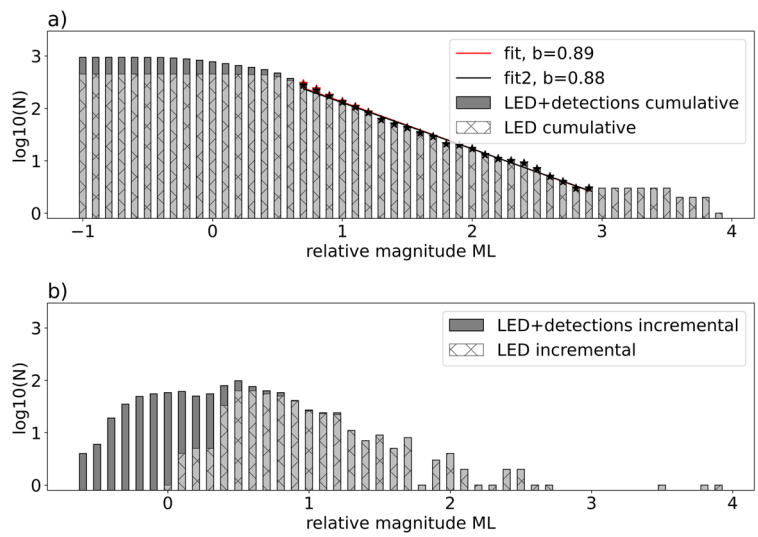

Fig. 22 Comparison of the a) cumulative and b) incremental magnitude-frequency distribution of the LED catalog 2018 - 2020 and complemented LED catalog 2018 - 2020 with the relative magnitudes of the detections (Bulletin-Files des Landeserdbebendienstes B-W 2011-2020). The red line gives the b-value fit of the magnitude-frequency distribution, determined using least squares fitting. The assumed M_c for the b-value fit is 0.6 and the width of the bars is 0.1 magnitude units

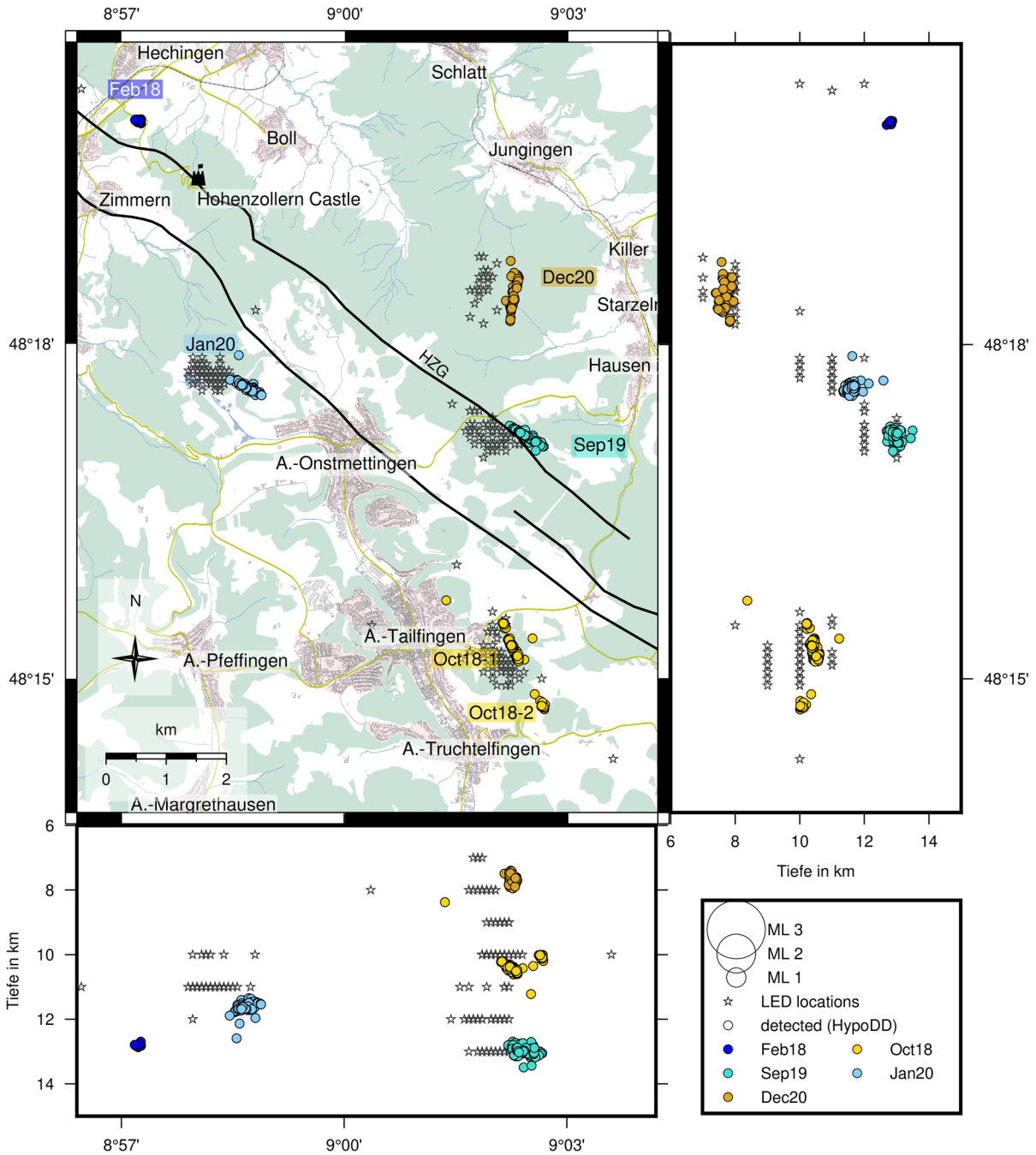

Fig. 23 HypoDD (circles) and LED (stars) hypocenter locations of the earthquake sequences Feb18, Oct18, Sep19, Jan20, and Dec20. Black lines indicate boundary faults of the Hohenzollerngraben (HZG, Regierungspräsidium Freiburg: Landesamt für Geologie, Rohstoffe und Bergbau (Hrsg.) 2019). Background map created with OpenStreetMap Data (2022, downloaded via geofabrik.de)

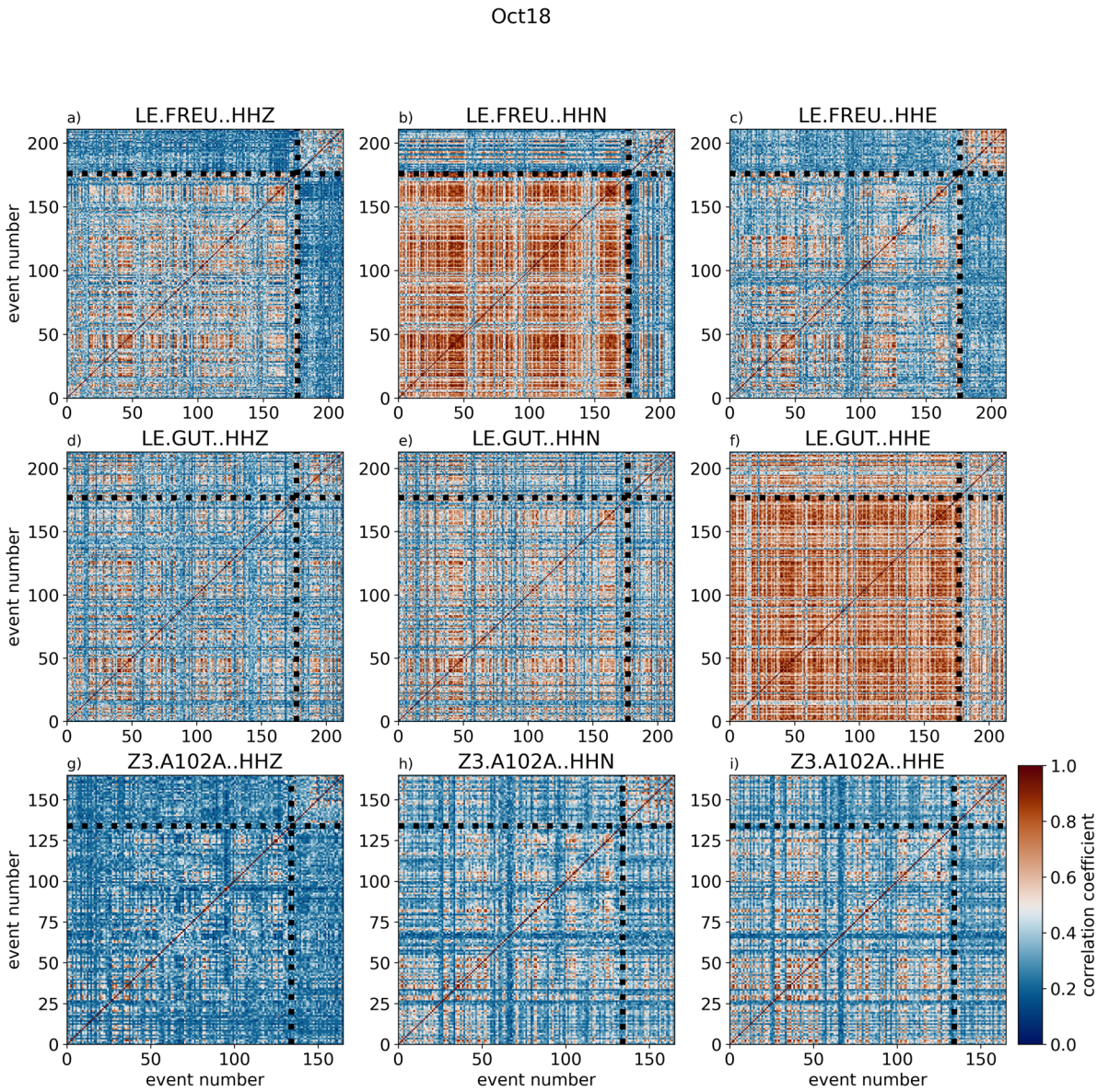

Fig. 24 Similarity matrices for the Oct18 earthquake sequence at the seismic stations FREU, GUT, and A102A based on waveform similarity. The station FREU is the closest station to the earthquake sequence location (about 7 km). Black dashed lines display the boundary between events in October 2018 to events in November 2018. Event number is consecutive with time

Acknowledgements We thank Stefan Stange, Martin Hensch and Jens Zeiss of the State Earthquake Service of Baden-Württemberg (Landeserdbebendienst B-W) for providing waveform data, pick files and internal information (Az4784//18_3303). Waveform recordings were provided by the AlpArray Seismic Network (2015). Recording instruments were provided by the KArlsruhe BroadBand Array, Karlsruhe Institute of Technology. Felix Bögelspacher, Felix Pappert, Leon Merkel, Sergio León-Ríos and Werner Scherer assisted the fieldwork. Michael Frietsch helped with the data management. Rune Helk determined phase arrival times on the StressTransfer and AlpArray seismic stations recordings. We thank numerous people and associations for supporting the installation of the mobile recording instruments on their land. We acknowledge support by the KIT-Library of the Karlsruhe Institute of Technology in connection with the DEAL-agreement. We thank Klaus Reicherter (Aachen) for support and discussions. We thank the AlpArray Seismic Network Team: György Hetényi, Rafael Abreu, Ivo Allegretti, Maria-Theresia Apoloner, Coralie Aubert, Simon Besançon, Maxime Bès de Berc, Götz Bokelmann, Didier Brunel, Marco Capello, Martina Čarman, Adriano Cavaliere, Jérôme Chèze, Claudio Chiarabba, John Clinton, Glenn Cougoulat, Wayne C. Crawford, Luigia Cristiano, Tibor Czifra, Ezio D'alema, Stefania Danesi, Romuald Daniel, Anke Dannowski, Iva Dasović, Anne Deschamps, Jean-Xavier Dessa, Cécile Doubre, Sven Egdorf, ETHZ-SED Electronics Lab, Tomislav Fiket, Kasper Fischer, Wolfgang Friederich, Florian Fuchs, Sigward Funke, Domenico Giardini, Aladino Govoni, Zoltán Gráczer, Gidera Gröschl, Stefan Heimers, Ben Heit, Davorka Herak, Marijan Herak, Johann Huber, Dejan Jarić, Petr Jedlička, Yan Jia, Hélène Jund, Edi Kissling, Stefan Klingen, Bernhard Klotz, Petr Kolínský, Heidrun Kopp, Michael Korn, Josef Kotek, Lothar Kühne, Krešo Kuk, Dietrich Lange, Jürgen Loos, Sara Lovati, Deny Malengros, Lucia Margheriti, Christophe Maron, Xavier Martin, Marco Massa, Francesco Mazzarini, Thomas Meier, Laurent Métral, Irene Molinari, Milena Moretti, Anna Nardi, Jurij Pahor, Anne Paul, Catherine Péquegnat, Daniel Petersen, Damiano Pesaresi, Davide Piccinini, Claudia Piromallo, Thomas Plenefisch, Jaroslava Plomerová, Silvia Pondrelli, Snježan Prevolnik, Roman Racine, Marc Régnier, Miriam Reiss, Joachim Ritter, Georg Rümpker, Simone Salimbeni, Marco Santulin, Werner Scherer, Sven Schippkus, Detlef Schulte-Kortnack, Vesna Šipka, Stefano Solarino, Daniele Spallarossa, Kathrin Spieker, Josip Stipčević, Angelo Strollo, Bálint Süle, Gyöngyvér Szanyi, Eszter Szücs, Christine Thomas, Martin Thorwart, Frederik Tilmann, Stefan Ueding, Massimiliano Vallocchia, Luděk Vecsey, René Voigt, Joachim Wassermann, Zoltán Wéber, Christian Weidle, Viktor Wesztergom, Gauthier Weyland, Stefan Wiemer, Felix Wolf, David Wolyniec, Thomas Zieke, Mladen Živčić and Helena Žlebčíková. The paper benefited from useful comments by the reviewers T. Diehl and M. Zeckra.

Author contributions Sarah Mader carried out the fieldwork of the StressTransfer Seismic Network, analyzed the data with self-written and open-source programs, and prepared the manuscript and figures. Joachim R. R. Ritter formulated the project, obtained funding and started the fieldwork of the StressTransfer Seismic Network. Andrea Brüstle provided on behalf of the LED the used LED event catalog and information regarding data processing at the LED. All three were involved in writing the manuscript. The AlpArray Working Group organized and coordinated the AlpArray Seismic Network operation.

Funding Information Open Access funding enabled and organized by Projekt DEAL. Sarah Mader and Joachim R. R. Ritter were supported by the Deutsche Forschungsgemeinschaft (DFG) through grant RI1133/13-1 within the framework of DFG Priority Programme "Mountain Building Processes in Four Dimensions (MB-4D)" (SPP 2017).

Availability of data and materials We used the earthquake catalog of the state earthquake service of Baden-Württemberg (LED) as well as permanent recordings of the LED seismic stations (Erdbebendienst Südwest Baden-Württemberg and Rheinland-Pfalz 2009), which were provided to us by the LED (Bulletin-Files des Landeserdbebendienstes B-W 2011-2020). Other permanent recordings, which are open access, are used from the Swiss Seismological Service (SED, Swiss Seismological Service (SED) at Eidgenössische Technische Hochschule (ETH) Zurich 1983), German Regional Seismic Network (GRSN, Federal Institute for Geosciences and Natural Resources (BGR) 1976), GEOFON seismic network (GEOFON Data Centre 1993), the AlpArray Seismic Network (AlpArray Seismic Network (AASN) 2015, Hetényi et al. 2018) and the StressTransfer Seismic Network (Mader and Ritter 2018, 2021).

Code availability The preprocessing, picking analyses and event detection were done in Python with the open-source toolbox ObsPy (Beyreuther et al. 2010) and the Python package EQcorrscan (Chamberlain et al. 2018). For further data analyses we used the freely available programs NonLinLoc (Lomax et al. 2000), FocMec (Snoke 2003) and HypoDD (Waldhauser and Ellsworth 2000). All figures were created with either the Matplotlib library in Python (Hunter 2007) or the Generic Mapping Tools (GMT, Wessel et al. 2019). For Figure 24 we used the color map vik of Crameri (2023).

Declarations

Competing interests The authors declare no competing interests.

References

Aichroth B, Prodehl C, Thybo H (1992) Crustal structure along the central segment of the EGT from seismic-refraction studies. Tectonophysics 207(1–2):43–64

AlpArray Seismic Network (AASN) (2015) AlpArray Seismic Network (AASN) temporary component. AlpArray Working Group. https://doi.org/10.12686/alparray/z3_2015

Beyreuther M, Barsch R, Krischer L et al (2010) ObsPy: A Python toolbox for seismology. Seismol Res Lett 81(3):530–533

Bhattacharya P, Viesca RC (2019) Fluid-induced aseismic fault slip outpaces pore-fluid migration. Science 364(6439):464–468

Bulletin-Files des Landeserdbebendienstes B-W (2011-2020) Ref. 98 im Landesamt für Geologie, Rohstoffe und Bergbau im Regierungspräsidium Freiburg, Az478418_3303

Čermáková H, Horálek J (2015) The 2011 West Bohemia (Central Europe) earthquake swarm compared with the previous swarms of 2000 and 2008. J Seismolog 19:899–913

Chamberlain CJ, Hopp CJ, Boese CM et al (2018) EQcorrscan: Repeating and near-repeating earthquake detection and analysis in Python. Seismol Res Lett 89(1):173–181

Crameri F (2023) Scientific colour maps (8.0.0). Zenodo. https://doi.org/10.5281/zenodo.8035877

Diehl T, Kissling E, Bormann P (2012) Tutorial for consistent phase picking at local to regional distances. In: Bormann P (ed) New Manual of Seismological Observatory Practice 2 (NMSOP-2). Potsdam, Deutsches GeoForschungsZentrum GFZ, pp 1–21

Diehl T, Madritsch H, Schnellmann M et al (2023) Seismotectonic evidence for present-day transtensional reactivation of the slowly deforming Hegau-Bodensee Graben in the northern foreland of the Central Alps. Tectonophysics 846:229659

Dublanchet P, De Barros L (2021) Dual seismic migration velocities in seismic swarms. Geophys Res Lett 48(1):e2020GL090025

Echtler HP, Chauvet A (1992) Carboniferous convergence and subsequent crustal extension in the southern Schwarzwald (SW Germany). Geodin Acta 5(1–2):37–49

El-Isa Z, Eaton DW (2014) Spatiotemporal variations in the b-value of earthquake magnitude-frequency distributions: Classification and causes. Tectonophysics 615–616:1–11

Erdbebendienst Südwest Baden-Württemberg and Rheinland-Pfalz (2009) Erdbebendienst Südwest [Data set]. https://doi.org/10.7914/SN/LE

Federal Institute for Geosciences and Natural Resources (BGR) (1976) German Regional Seismic Network (GRSN). Federal Institute for Geosciences and Natural Resources (BGR). https://doi.org/10.25928/mbx6-hr74

Fonsêca J, Ferreira J, do Nascimento A et al (2021) Intraplate earthquakes in the Potiguar Basin, Brazil: Evidence for superposition of local and regional stresses and implications for moderate-size earthquake occurrence. J S Am Earth Sci 110:103370

Frohlich C, Davis SD (1993) Teleseismic b values; or, much ado about 1.0. J Geophys Res Solid Earth 98(B1):631–644

Gajewski D, Prodehl C (1985) Crustal structure beneath the Swabian Jura, SW Germany, from seismic refraction investigations. J Geophys 56(2):69–80

GEOFON Data Centre (1993) GEOFON Seismic Network. Deutsches GeoForschungsZentrum GFhttps://doi.org/10.14470/TR560404

Grünthal G, Stromeyer D, Bosse C et al (2018) The probabilistic seismic hazard assessment of Germany-version 2016, considering the range of epistemic uncertainties and aleatory variability. Bull Earthq Eng 16:4339–4395

Haessler H, Hoang-Trong P, Schick R et al (1980) The September 3, 1978, Swabian Jura earthquake. Tectonophysics 68:1–14

Hainzl S (2004) Seismicity patterns of earthquake swarms due to fluid intrusion and stress triggering. Geophys J Int 159(3):1090–1096

Hainzl S, Ogata Y (2005) Detecting fluid signals in seismicity data through statistical earthquake modeling. J Geophys Res Solid Earth 110(B5)

Hann HP, Chen F, Zedler H et al (2003) The Rand Granite in the southern Schwarzwald and its geodynamic significance in the Variscan belt of SW Germany. Int J Earth Sci 92:821–842

Heidbach O, Rajabi M, Reiter K, et al (2016) World Stress Map Database Release 2016, V. 1.1. GFZ Data Servicehttps://doi.org/10.5880/WSM.2016.001

Hetényi G, Molinari I, Clinton J et al (2018) The AlpArray Seismic Network - a large scale European experiment to image the Alpine orogen. Surv Geophys 39:1009–1033

Hunter JD (2007) Matplotlib: a 2D graphics environment. Comput Sci Eng 9:90–95

Hürtgen J, Reicherter K, Spies T, et al (2020) The Paleoseismic Database of Germany and Adjacent Regions PalSeisDB v1.0. Historical Earthquakes, Paleoseismology, Neotectonics and Seismic Hazard: New Insights and Suggested Procedures. pp 73–136

Illies JH (1982) Der Hohenzollerngraben und Intraplattenseismizität infolge Vergitterung lamellärer Scherung mit einer Riftstruktur. Oberrhein Geol Abh 31:47–78

Kastrup U, Zoback ML, Deichmann N et al (2004) Stress field variations in the Swiss Alps and the northern Alpine foreland derived from inversion of fault plane solutions. J Geophys Res 109(B01402). https://doi.org/10.1029/2003JB002550

Kissling E, Schlunegger F (2018) Rollback orogeny model for the evolution of the Swiss Alps. Tectonics 37:1097–1115

Lohman RB, McGuire JJ (2007) Earthquake swarms driven by aseismic creep in the Salton Trough, California. J Geophys Res Solid Earth 112(B4)

Lomax A, Virieux J, Volant P, et al (2000) Probabilistic earthquake location in 3D and layered models: introduction to a Metropolis-Gibbs method and comparison with linear locations. In: Thurber C, Rabinowitz N (eds) Advances in seismic event location. Springer, p 101–134

Mader S, Ritter JRR (2018) StressTransfer [Data set]. International Federation of Digital Seismograph Network. https://doi.org/10.7914/SN/5N_2018

Mader S, Ritter JRR (2021) The StressTransfer Seismic Network - An Experiment to Monitor Seismically Active Fault Zones in the Northern Alpine Foreland of Southwestern Germany. Seismol Res Lett 92(3):1773–1787

Mader S, Ritter JRR, Reicherter K et al (2021) Seismicity and seismotectonics of the Albstadt Shear Zone in the northern Alpine foreland. Solid Earth 12(6):1389–1409

Mogi K (1962) Magnitude-frequency relation for elastic shocks accompanying fractures of various materials and some

related problems in earthquakes (2nd paper). Bull Ocean Res Inst Univ Tokyo 40:831–853
Mogi K (1963) Some discussions on aftershocks, foreshocks and earthquake swarms: the fracture of a semi-infinite body caused by an inner stress origin and its relation to the earthquake phenomena (third paper). Bull. Ocean Res Inst Univ Tokyo 41:615–658
Müller B, Zoback ML, Fuchs K et al (1992) Regional patterns of tectonic stress in Europe. J Geophys Res Solid Earth 97(B8):11783–11803
Piña-Valdés J, Socquet A, Beauval C et al (2022) 3D GNSS velocity field sheds light on the deformation mechanisms in Europe: Effects of the vertical crustal motion on the distribution of seismicity. J Geophys Res Solid Earth 127(6):e2021JB023451
Regierungspräsidium Freiburg: Landesamt für Geologie, Rohstoffe und Bergbau (Hrsg.) (2019) LGRB-Kartenviewer - Layer GüK300:Tektonik. Available at: https://maps.lgrb-bw.de/, Last Access: 28 Mar 2019
Reicherter K, Froitzheim N, Jarosiński, et al (2008) Alpine tectonics north of the Alps. In: McCann T (ed) The Geology of Central Europe, vol 2, Mesozoic and Cenozoic. Geological Society of London, chap 19, pp. 1233–1286
Reinecker J, Schneider G (2002) Zur Neotektonik der Zollernalb: Der Hohenzollerngraben und die Albstadt-Erdbeben. Jahresberichte und Mitteilungen des Oberrheinischen Geologischen Vereins 84:391–417
Reinecker J, Tingay M, Müller B et al (2010) Presentday stress orientation in the Molasse basin. Tectonophysics 482:129–138
Reiter K, Heidbach O, Müller B, et al (2016) Stress Map Germany 2016.https://doi.org/10.5880/WSM.Germany2016_en
Röckel L, Ahlers S, Müller B et al (2022) The analysis of slip tendency of major tectonic faults in Germany. Solid Earth 13(6):1087–1105
Roland E, McGuire JJ (2009) Earthquake swarms on transform faults. Geophys J Int 178(3):1677–1690
Rupf I, Nitsch E (2008) Das Geologische Landesmodell von Baden-Württemberg: Datengrundlagen, technische Umsetzung und erste geologische Ergebnisse. Regierungspräsidium Freiburg–Abteilung 9, Landesamt für Geologie, Rohstoffe und Bergbau. Available at https://produkte.lgrb-bw.de/schriftensuche/lgrb-informationen/informationen21?term=Landesmodell (Last accessed March 2021)
Schädel K (1976) Geologische übersichtskarte, 1:100.000 C7918 Albstadt und Erläuterungen. Geologisches Landesamt Baden-Württemberg, Freiburg im Breisgau, pp 44
Schaff DP, Richards PG (2014) Improvements in magnitude precision, using the statistics of relative amplitudes measured by cross correlation. Geophys J Int 197(1):335–350
Schneider G (1979) The earthquake in the Swabian Jura of 16 November 1911 and present concepts of seismotectonics. Tectonophysics 53(3–4):279–288
Schwarz J, Beinersdorf S, Meidow H (2019) Magnitudenorientierter Erdbebenkatalog für deutsche und angrenzende Gebiete EKDAG - erweiterter Ahorner-Katalog. Bauhaus Universitätsverlag
Shapiro SA, Dinske C (2009) Scaling of seismicity induced by nonlinear fluid-rock interaction. J Geophys Res Solid Earth 114(B9)
Shelly DR, Hardebeck JL (2010) Precise tremor source locations and amplitude variations along the lower-crustal central San Andreas Fault. Geophys Res Lett 37(L14301)
Sieberg A, Lais R (1925) Das mitteleuropäische Erdbeben vom 16. November 1911, Beartbeitung der makroseismichen Beobachtungen. In: Hecker O (ed) Veröffentlichungen der Reichsanstalt für Erdbebenforschungen in Jena, vol 4. Gustav Fischer, Jena, p 106
Singer J, Diehl T, Husen S et al (2014) Alpine lithosphere slab rollback causing lower crustal seismicity in northern foreland. Earth Planet Sci Lett 397:42–56
Snoke JA (2003) FOCMEC: Focal mechanism determinations. In: Lee WH, Kanamori H, Jennings P et al (eds) International Handbook of Earthquake & Engineering Seismology, Part B. Academic Press, San Diego, pp 1629–1630
Stange S, Brüstle W (2005) The Albstadt/Swabian Jura seismic source zone reviewed through the study of the earthquake of March 22, 2003. Jahresberichte und Mitteilungen des Oberrheinischen Geologischen Vereins 87:391–414
Swiss Seismological Service (SED) at Eidgenössische Technische Hochschule (ETH) Zurich (1983) National Seismic Networks of Switzerland. ETH Zürich. https://doi.org/10.12686/sed/networks/ch
Talwani P (1988) The intersection model for intraplate earthquakes. Seismol Res Lett 59(4):305–310
Tozer B, Sandwell DT, Smith WH et al (2019) Global bathymetry and topography at 15 arc sec: SRTM15+. Earth Space Sci 6(10):1847–1864
Tron V, Brun JP (1991) Experiments on oblique rifting in brittle-ductile systems. Tectonophysics 188(1–2):71–84
Truttmann S, Diehl T, Herwegh M (2023) Hypocenter-based 3D Imaging of active faults: method and applications in the Southwestern Swiss Alps. J Geophys Res Solid Earth 128(6):e2023JB026352
Turnovsky J (1981) Herdmechanismen und Herdparameter der Erdbebenserie 1978 auf der Schwäbischen Alb. PhD thesis, University Stuttgart, Germany, pp 109
Tyagunov S, Grünthal G, Wahlström R et al (2006) Seismic risk mapping for Germany. Nat Hazard 6(4):573–586. https://doi.org/10.5194/nhess-6-573-2006
Waldhauser F, Ellsworth WL (2000) A double-difference earthquake location algorithm: Method and application to the northern Hayward fault, California. Bull Seismol Soc Am 90(6):1353–1368
Wells DL, Coppersmith KJ (1994) New Empirical Relationships among Magnitude, Rupture Length, Rupture Width, Rupture Area and Surface Displacement. Bull Seismol Soc Am 84(4):974–1002
Wessel P, Luis JF, Uieda L et al (2019) The Generic Mapping Tools version 6. Geochem Geophy Geosys 20:5556–5564